Research Article
Journal of Geophysical Research: Oceans
DOI 10.1002/2017JC013534

Dynamic topography and sea level anomalies of the Southern Ocean: Variability and teleconnections

Thomas W. K. Armitage[1], Ron Kwok[1], Andrew F. Thompson[2], and Glenn Cunningham[1]

[1]Jet Propulsion Laboratory, California Institute of Technology, Pasadena, California, USA.

[2]Environmental Science and Engineering, California Institute of Technology, Pasadena, California, USA

Corresponding author: T. Armitage (Tom.W.Armitage@jpl.nasa.gov)

Key Points:

- New monthly merged sea level record of the ice-covered and ice-free Southern Ocean between 2011-2016, from CryoSat-2 radar altimetry
- Antarctic coastal sea level peaks in autumn, minimum in spring; Antarctic Slope Current speeds regionally up to twice as fast in autumn
- Southern Oscillation and Southern Annular Mode drive significant Antarctic coastal sea level response, modulating the ASC strength

Received: Oct 05, 2017; Revised: Dec 04, 2017; Accepted: Jan 02, 2017

Abstract

This study combines sea surface height (SSH) estimates of the ice-covered Southern Ocean with conventional open ocean SSH estimates from CryoSat-2 to produce monthly composites of dynamic ocean topography (DOT) and sea level anomaly (SLA) on a 50km grid spanning 2011-2016. This dataset reveals the full Southern Ocean SSH seasonal cycle for the first time; there is an antiphase relationship between sea level on the Antarctic continental shelf and the deeper basins, with coastal SSH highest in autumn and lowest in spring. As a result of this pattern of seasonal SSH variability, the barotropic component of the Antarctic Slope Current (ASC) has speeds that are regionally up to twice as fast in the autumn. Month-to-month circulation variability of the Ross and Weddell Gyres is strongly influenced by the local wind field, and is correlated with the local wind curl (Ross: -0.58; Weddell: -0.67). SSH variability is linked to both the Southern Oscillation and the Southern Annular Mode, dominant modes of southern hemisphere climate variability. In particular, during the strong 2015-2016 El Niño, a sustained negative coastal SLA of up to -6cm, implying a weakening of the ASC, was observed in the Pacific Sector of the Southern Ocean. The ability to examine sea level variability in the seasonally ice-covered regions of the Southern Ocean – climatically important regions with an acute sparsity of data – makes this new merged sea level record of particular interest to the Southern Ocean oceanography and glaciology communities.

1 Introduction

The Southern Ocean encircles the Antarctic continent and will be defined in this study as the ocean regions south of 40°S (Figure 1). The Atlantic, Indian and Pacific sectors of the Southern Ocean are found between Drake Passage (~67°W) and 20°E, between 20°E and 150°E and between 150°E and Drake Passage, respectively. The absence of a land mass connecting Antarctica to other continents – forming a zonal band uninterrupted by land between ~56-61°S – allows the strong westerly wind stress and surface buoyancy forcing to generate the Antarctic Circumpolar Current (ACC) [*Hogg*, 2010], associated with some of the strongest currents on Earth as well as the ventilation of deep water masses. Transport estimates for the ACC range from historical estimates similar to the 134 Sv estimated by *Cunningham et al.* [2003], while more recent studies suggest that it could be as large as 173 Sv [*Donohue et al.*, 2016] (1 Sv ≡ 10^6 m^3 s^{-1}). The ACC permits the exchange of water masses between different ocean basins; this zonal component of the circulation is a key aspect of the global overturning circulation [*Lumpkin and Speer*, 2007; *Talley*, 2013; *Jones and Cessi*, 2016; *Thompson et al.*, 2016]. Further south, near-shore easterly winds drive on-shore Ekman transport, deepening isopycnals and raising sea levels near the coast, which gives rise to the westward flowing Antarctic Slope Current (ASC).

The ASC has traditionally been described as a wind-driven, topographically-controlled current [*Gill*, 1973] that follows the continental shelf edge westwards (Figure 1), occupying an important region for water mass transformation, surface buoyancy and momentum fluxes, sea ice formation and input of terrestrial ice [*Jacobs*, 1991]. While it has historically been poorly observed, recent results from high-resolution ocean modelling suggest that the ASC is strongly influenced by the local wind stress in terms of both its mean flow and seasonal variability [*Mathiot et al.*, 2011], findings supported by moored observations in the southern Weddell Gyre

[*Nunez-Riboni and Fahrbach*, 2009]. The ASC is strongest in coastal East Antarctica and weakest in West Antarctic, in particular along the Western Antarctic Peninsula, however its full extent and variability are not well observed. It has been suggested that poleward shifting westerlies under climate change will modify the ASC and the associated on-shore Ekman transport, changing ocean temperatures at 200-700m depths that could influence glacial melt [*Spence et al.*, 2014; *Goddard et al.*, 2017; *Spence et al.*, 2017]. The ASC also forms the southern boundaries of the cyclonic Ross and Weddell Sea Gyres. The eastward flow along the northern boundary of the Ross Gyre coincides with the southern boundary of the ACC, whereas in the Weddell Gyre, the gyre's northern boundary is separated from the ACC by the South Scotia Ridge and the Southwest Indian Ridge [*Heywood et al.*, 2004]. Despite a paucity of data in the marginal seas of Antarctica, there is evidence that the Ross Sea has freshened since the 1950s, postulated to be associated with increased melt of terrestrial ice [*Jacobs and Giulivi*, 2010]. Meanwhile, water on the continental shelves of the Amundsen and Bellingshausen Seas has warmed, linked to shoaling of the mid-depth temperature maximum over the continental slope, leading to an enhanced delivery of warm water to both the continental shelf and to ice shelf cavities in these regions [*Schmidtko et al.*, 2014]. Much of our understanding of Antarctica's marginal circulation has been patched together from various observational programs, and a comprehensive view of the spatial and temporal variability of this surface circulation has remained out of reach.

Over most of the global ocean, satellite radar altimeter measurements have provided regular estimates of sea surface height and surface geostrophic circulation since the early 1990s [*Cazenave et al.*, 2014]. Yet, extensive, year-round, long-term SSH observations are limited by the presence of sea ice, which, at its maximum extent, covers around 19 million square kilometers of the Southern Ocean [*Fetterer et al.*, 2016], obscuring the ocean surface of the marginal seas and the Ross and Weddell Gyres (Figure 1, yellow contour). Even during summer months, some 3 million square kilometers of perennial sea ice remains, predominantly in the Weddell and Ross Seas. There have been a few attempts to obtain localized records of SSH variability around the Antarctic margins. For example, *Rye et al.* [2014] utilized the available open-ocean altimeter SSH record and found that summertime sea levels for the seasonally ice-free regions of the Southern Ocean are rising 2 mm/year faster than the regional mean south of 50°S, which they attributed to increased terrestrial freshwater input. However, the failure of conventional altimeter processing in the presence of sea ice means that the data used by *Rye et al.* [2014] does not capture seasonal sea level variability and omits regions of perennial ice cover entirely. In recent years, methods have been developed to estimate SSH from radar altimetry in the ice-covered ocean by picking out returns that originate from openings in the sea ice cover [*Laxon and Mcadoo*, 1994; *Peacock and Laxon*, 2004; *Kwok and Morison*, 2011; *Farrell et al.*, 2012; *Giles et al.*, 2012; *Bulczak et al.*, 2015; *Armitage et al.*, 2016; *Kwok and Morison*, 2016; *Mizobata et al.*, 2016]. SSH estimates from ice-covered regions have also been combined with conventional open ocean SSH estimates to produce basin-wide composites of Arctic Ocean SSH at annual [*Giles et al.*, 2012] and monthly [*Armitage et al.*, 2016] timescales. In the Arctic, these combined datasets have been used to study year-round SSH variability for the first time, to estimate freshwater distribution and storage, examine changing surface geostrophic circulation and to make estimates of Arctic Ocean eddy kinetic energy [*Giles et al.*, 2012; *Armitage et al.*, 2016; *Armitage et al.*, 2017]. Monthly Arctic Ocean altimeter SSH estimates have been compared with tide gauges in seasonally ice-covered seas, with regional correlation ranging from R=0.89 in the Barents Sea to R=58 in the Laptev and East Siberian Seas [*Armitage et al.*, 2016], as well as against steric height estimated hydrographic observations within the ice pack, with correlation of R~0.9 [*Armitage et al.*, 2016; *Kwok and Morison*, 2016]. Further, *Armitage et al.* [2017] found that altimeter-derived surface geostrophic currents captured the monthly mean surface current speed and direction observed by moorings in the Beaufort Sea within ~1-2 cm/s and ~60° RMS difference. Overall, these results lend confidence to the technique of combining data from the open ocean and ice-covered ocean in this way.

Basin-wide observations of Southern Ocean SSH and surface geostrophic circulation would allow us to study and to monitor key aspects of ocean variability in the Antarctic marginal seas, the ASC, and the Ross and Weddell Gyres, to better understand these climatically important regions. Recently, *Kwok and Morison* [2016] presented SSH estimates for the ice-covered Southern Ocean. This study extends the radar altimeter techniques developed in the Arctic Ocean to combine these SSH estimates with conventional open-ocean SSH retrievals to produce composites of basin-wide Southern Ocean SSH, covering both ice-covered and ice-free regions, between 2011-2016, with monthly resolution. This allows us to examine Southern Ocean SSH and surface circulation variability down to seasonal timescales, in particular in the Antarctic marginal seas and the Ross and Weddell Gyres, which are ice-covered during the winter, and largely ice-free during the summer: the SSH record developed here is a unique tool for examining seasonal variability in these regions, where previous records only cover either the ice-covered (e.g., *Kwok and Morison* [2016]) or ice-free periods of the year (e.g., [*Rye et al.*, 2014]). Section 2 outlines the data used and methodology; Section 3 examines the time-mean dynamic ocean topography, the seasonal variability and strength of the Ross and Weddell gyres, and the influence of large scale climate modes on Southern Ocean sea level; Section 4 provides some discussion and context for the results; and we conclude in Section 5.

2 Data and Methods

2.1 Sea surface height

The SSH data presented here were derived using radar altimetry data from the CyroSat-2 (CS-2) mission [*Wingham et al.*, 2006]. This study combines monthly estimates of CS-2 SSH in the ice-covered regions of the Southern Ocean with conventional radar altimeter estimates of

SSH from the ice-free regions between 2011-2016. Accurate SSH retrievals in ice-covered portions of the ocean require two important processing choices: first, distinguishing between specular echoes originating from leads, from which SSH can be estimated, and more diffuse echoes originating from sea ice floes; and second, re-tracking the lead returns to estimate SSH [*Laxon*, 1994; *Peacock and Laxon*, 2004; *Kwok and Morison*, 2016]. While there are different methodologies for both of these steps, here we estimate SSH in ice-covered regions using the method described in detail by *Kwok and Morison* [2016]. The exposed ocean surface in openings in the sea ice cover is typically very flat, and as such appears as a very bright (specular) reflective surface to radar altimeters. Radar echoes originating from openings in the sea ice cover are characterized by high peak power and are very narrow, so they are identified through a combination of the echo peak power and the width at the half-power point on the leading edge (the first arrival from the surface); echoes originating from leads can be identified as those echoes with high peak power and a narrow leading-edge width. The retracking point – the point on the echo that corresponds to the mean surface elevation – is then taken to be the half-power point on the leading edge. Readers interested in the low-level altimeter processing are directed to *Kwok and Morison* [2016], where this methodology is described in detail.

Over the open ocean we make use of CS-2 data processed and archived in the Radar Altimeter Database System (RADS) [*Scharroo et al.*, 2013a]. Over much of the open ocean, CS-2 operates as a conventional pulse limited radar altimeter, switching to Synthetic Aperture Radar (SAR) mode close to the sea ice edge, as well as in selected experimental areas of the open ocean. In RADS, CS-2 SAR mode data is 'downgraded' to pseudo-pulse limited data, by not applying the slant-range correction to align the Doppler beams in time [*Scharroo et al.*, 2013b]. In this way, both pulse limited and SAR data can be treated consistently in RADS and are retracked with the MLE3 model fit retracker [*Scharroo et al.*, 2013b], thereby providing data up until CS-2 intercepts the sea ice edge, after which the conventional processing fails and the data is flagged invalid.

The dynamic ocean topography (DOT) is the SSH relative to the geoid, defined as:

$$H_{DOT} = H_{SSH} - H_{geoid} = A - \left(R + \sum H_{corr}\right) - H_{geoid} \#(1)$$

where H_{SSH} is the SSH relative to the World Geodetic System 1984 (WGS84) ellipsoid, H_{geoid} is the geoid height, A is the satellite altitude relative to the WGS84 ellipsoid, R is the retracked range to the surface and $\sum H_{corr}$ is the sum of atmospheric path delay and tidal corrections. All the standard geophysical corrections are applied: the dry and wet troposphere, ionosphere, ocean tide, long period tide, solid Earth tide and geocentric polar tide corrections are applied globally; the dynamic atmosphere correction and sea state bias are applied only over the open ocean; and the inverse barometer correction is applied only in ice-covered regions. SSH was referenced to the GOCO05c combined gravity field model to derive DOT [*Fecher et al.*, 2017]. GOCO05c contains the full mission lifetime of Gravity Field and Steady-State Ocean Circulation Explorer (GOCE) data, with improved data quality when compared to other state-of-the-art gravity models (e.g., EGM2008; Figure 3c-e) in the coastal regions of Antarctica. GOCE currently provides the highest resolution and most accurate gravity data in these regions where other data sources are not available. Pointwise data are projected into polar stereographic coordinates [*Snyder*, 1987] using the mapping parameters of the SSM/I grid documented by the National Snow and Ice Data Center (nsidc.org/data/polar-stereo/ps_grids.html). To avoid land contamination, pointwise data are discarded if they fall within 10km of land or ice shelves – this step is especially important for accurate SSH retrievals in proximity to the myriad small island chains of the Southern Ocean.

The next stage in producing a consistent combined ice-covered and open ocean dataset is to level the various data sets against each other. In coastal regions of Antarctica, CS-2 operates in SAR interferometric (SARIN) mode [*Wingham et al.*, 2006] and this data is first leveled against the adjacent SAR mode data. While in principle, SAR and SARIN data should not need levelling, there are known residual range biases in the SAR/SARIN mode data [*Scagliola and Fornari*, 2017]. Furthermore, the increased noise in SARIN mode data relative to SAR mode (only one quarter as many pulses are accumulated in SARIN mode) means that the leading-edge tracker may systematically underestimate the range compared to SAR mode. After levelling the SAR and SARIN mode data, the ice-covered data is leveled against the open ocean data from RADS. The levelling procedure follows *Armitage et al.* [2016]:

1. The ice-covered SAR and SARIN data are averaged separately on a 50km stereographic grid and differenced to produce a set of gridded monthly differences. We calculate the monthly area-averaged difference for all grid cells within our study region (Figure 1), although in reality only grid cells close to the Antarctic coast, where CS-2 changes mode, contain valid differences. We then average the monthly area-averaged differences to obtain a single time-mean difference, which is removed from the pointwise SARIN data.
2. This step is repeated for the ice-covered and open ocean datasets, where this time the monthly difference grids only contain valid differences close to the ice edge at the transition between the open ocean and ice-covered datasets, and the time-mean difference is removed from the pointwise ice-covered data.

3. The pointwise ice-covered (SAR & SARIN) and ice-free data are then combined into initial monthly DOT composites, which are time-averaged to produce an initial 2011-2016 mean DOT field.
4. The initial mean DOT is subtracted from the monthly pointwise data to produce sea level anomalies (SLA).
5. Steps 1 & 2 are repeated using SLA in place of DOT, in order to remove the effect of sub-grid cell dynamic topography variations on the computed differences. Absolute sea level anomalies greater than 100cm are discarded (this step is important to remove any remaining land-contaminated data) and the mean differences are removed.
6. The pointwise ice-covered (SAR & SARIN) and ice-free data are then combined to produce monthly composites of DOT at 50km resolution using nearest neighbor gridding and smoothed with a Gaussian weighted filter with a radius of 80km [*Wessel et al.*, 2017]. A final 2011-2016 mean DOT is computed and this is removed from the monthly DOT maps to produce monthly SLA estimates.

Figure 2 shows the additional coverage provided by combining the conventional RADS open ocean SSH estimates with the ice-covered SSH estimates. There is a vast improvement of data coverage in the seasonally ice-covered region of the Southern Ocean, particularly in the Weddell Sea, where extensive sea ice cover persists throughout the year. While the improvement in coverage close to the coast is primarily due to the inclusion of SSH estimates in the ice-covered ocean, RADS does not include CS-2 data where the instrument is operated in SARIN mode, unlike the SSH estimates of *Kwok and Morison* [2016]. In fact, the lack of SARIN mode data in RADS accounts for almost all of the remaining data gaps in the monthly composites

(Figure 2b), visible as regions of the open ocean with lower data coverage (warmer colors in Figure 2), particularly off the coast of the western Antarctic Peninsula.

2.2 ERA-Interim reanalysis

The altimeter-derived SLA time series is compared against sea level pressure (SLP) and 10-m vector wind fields from the ERA-Interim Reanalysis [*Dee et al.*, 2011], to investigate the influence of atmospheric forcing on Southern Ocean sea level. Monthly mean wind fields were taken from the ERA-Interim portal (http://apps.ecmwf.int/datasets/data/interim-full-moda/levtype=sfc/). The data are provided on a 0.75° longitude-latitude grid, which was re-gridded to the same 50km SSM/I polar stereographic grid as the altimeter data by nearest neighbor interpolation [*Wessel et al.*, 2017].

2.3 Climate indices

The altimeter-derived SLA and ERA-Interim atmospheric fields are compared against two large-scale southern hemisphere climate indices: The Southern Oscillation Index (SOI) and the Southern Annular Mode (SAM). The SOI captures large-scale variations in atmospheric pressure between the eastern and western Pacific Ocean that are associated with El Niño and La Niña cycles. While the Southern Oscillation is principally associated with atmospheric variability at tropical latitudes, it is known that there is an imprint of the Southern Oscillation in atmospheric pressure (and hence surface winds) in the South Pacific Ocean, which drives variability in regional sea ice edge contraction/expansion by wind forcing [*Kwok et al.*, 2017; *Pope et al.*, 2017]. Further, La Niña events have been implicated in the delivery of oceanic heat to ice shelf cavities in the Amundsen Sea by regulating along-shore winds and their subsequent impact on the vertical structure of ocean properties at the shelf break and over the continental shelf [*Dutrieux et al.*, 2014]. We take the monthly SOI from the NOAA National Centers for Environmental Information (www.ncdc.noaa.gov/teleconnections/enso/indicators/soi/).

The SAM is the leading mode of southern hemisphere atmospheric variability for multiple parameters including surface pressure, geopotential heights, surface temperature, and zonal winds [*Thompson and Wallace*, 2000; *Marshall*, 2003]. It is associated with zonally-symmetric (annular) atmospheric anomalies that are of opposite signs between Antarctica and mid-latitudes. Positive phases of the SAM are associated with negative atmospheric pressure anomalies around Antarctica relative to mid-latitudes, and a contraction and strengthening of the associated westerly winds, while negative SAM phases are associated with an expansion and weakening of the westerlies. The SAM has been implicated in sea ice drift and extent variability [*Kwok et al.*, 2017; *Turner et al.*, 2017], and the study of *Spence et al.* [2014] found that the decadal positive trend in the SAM and the associated contraction of westerlies may be weakening the ASC and increasing oceanic heat at intermediate depths. Here, we use the SAM index provided by the British Antarctic Survey (https://legacy.bas.ac.uk/met/gjma/sam.html) produced using the methodology of [*Marshall*, 2003]; this index is calculated as the difference in normalized zonal mean sea level pressure between two sets of stations roughly centered on 40°S and 65°S.

2.4 Climate index composites

Sea level and surface atmospheric forcing anomaly composites are constructed for the positive and negative phases of the SOI and SAM. The climate indices are first re-normalized to have zero mean and a standard deviation of one between 2011-2016, and their seasonal cycle is removed. We subtract the 2011-2016 mean SLP and wind components to derive atmospheric anomalies. Then, gridded monthly climatologies of SLA, SLP, and 10-m wind between 2011 and 2016 are constructed, and the monthly climatology is subtracted from each anomaly dataset, to remove the seasonal cycle. By removing the seasonal cycle from the climate indices, as well as the gridded fields, we remove any seasonal co-variability between the datasets that could lead to spurious correlations. Finally, the monthly SOI and SAM composites are the positive and negative climate-index-weighted mean sea level, SLP and 10-m wind anomalies. Computing the SOI and SAM composites in this way places emphasis on months with larger absolute values of the climate indices and also captures any asymmetry between the response to positive and negative extremes, which would not be captured by a simple linear regression of the gridded fields against the climate indices. We also compute the linear correlation between the climate indices and the sea level, SLP and 10-m wind anomalies to determine regions of statistically significant climate forcing influence. Given the relative consistency in the large-scale atmospheric response of several different reanalyses to the climate indices (Figures S2-S5), we expect the choice of reanalyses to have negligible effect on the present analysis.

3 Results

This section presents the results of our analysis of the DOT/SLA fields described in Section 2.1. Section 3.1 presents the mean Southern Ocean dynamic topography and geostrophic currents for this period, as well as the impact of the geoid model used to estimate DOT. Section 3.2 discusses the mean state, seasonal variability and strength of the Ross and Weddell Gyres and Section 3.3 examines the response of Southern Ocean sea level to forcing by the Southern Annular Mode and the Southern Oscillation.

3.1 2011-2016 mean DOT

The Southern Ocean mean DOT for 2011-2016 shows the typical deep trough surrounding the Antarctic continent (Figure 3a). Figure 3c shows the difference between the mean DOT calculated relative to the GOCO05c and EGM2008 geoid models for the Weddell Sea sector. The largest differences are at spatial wavelengths of ~100km reflecting the value added by the inclusion of GOCE data over just GRACE at spherical harmonic degrees 150-180 [*Pail et al.*, 2010]. Over the Antarctic continent, the only data in EGM2008 comes from GRACE, which has a ground resolution of ~300km, and, additionally, the conventional open ocean altimetry data used in EGM2008 suffers from a lack of coverage in Antarctic marginal seas owing to the presence of sea ice [*Pavlis et al.*, 2013]. Thus, the difference between the geoid models is greatest in the marginal seas of Antarctica, close to the coast, where the inclusion of GOCE data has the greatest impact. Geostrophic currents, $\underline{\boldsymbol{u}}_{\boldsymbol{g}}$, are estimated as:

$$\underline{\boldsymbol{u}}_{\boldsymbol{g}} = \frac{f}{g}\left(\widehat{\boldsymbol{k}} \times \nabla_H H_{DOT}\right) \#(2)$$

where $f = 2\Omega \sin\phi$ is the Coriolis frequency, Ω is the Earth's rotation rate, ϕ is the latitude, g is the acceleration due to gravity, $\widehat{\boldsymbol{k}}$ is the unit vector normal to the geoid, $\nabla_H = (\partial/\partial x\,, \partial/\partial y\,, 0)$ is the horizontal gradient operator and H_{DOT} is the DOT estimated from Equation (1) (Figure 3b). The improvement offered by the GOCO05c geoid is particularly evident in the geostrophic current speed fields (Figure 3d & e) within ~300km of the Antarctic coastline. The currents calculated using EGM2008 (Figure 3e) show unresolved geoid features, evidenced by the typical 'ringing' features characteristic of the spherical harmonic representation used by geoid models.

While this noise near the coast is not wholly removed in the currents estimated using GOCO05c (Figure 3d), the improvement is clear from visual inspection alone.

While the dynamical link between SSH and the ACC is well-described in the literature (e.g. [*Orsi et al.*, 1995; *Sokolov and Rintoul*, 2009; *Kim and Orsi*, 2014]), the seasonally ice-covered seas of the Southern Ocean surrounding Antarctica are less well-documented. In the center of the Ross and Weddell Gyres, the mean DOT field is extremely flat, with mean current speeds of less than 0.5 cm/s over large areas. The DOT changes by around 2m from the northern boundary of the ACC, moving southwards towards Antarctica, with the center of the Weddell Gyre marking the lowest point in the global DOT. The higher DOT close to the Antarctic continent supports the ASC, and is revealed here to be an almost circumpolar feature of the Southern Ocean circulation. Mean current speeds in the ASC range from 2-10 cm/s, but are strongest in the eastern Ross, Mawson, Cooperation, and Riiser-Larsen Seas. The mean DOT and sea level variability in the Ross and Weddell Gyre regions, as well as seasonality of the ASC, is discussed in greater detail in the following sections.

3.2 Ross and Weddell Gyre sea level variability

A seasonal SLA climatology was constructed from the six years of data by averaging the monthly data by season - January-March (JFM), April-June (AMJ), July-September (JAS) and October-December (OND) - for the Ross gyre region (Figure 4) and the Weddell gyre region (Figure 5). We also compute the 'depth' of the Ross and Weddell Gyres to characterize the strength of the gyre circulation and compare this with the wind curl to investigate the role of wind forcing (Figure 6). The Ross Gyre depth is calculated as the monthly mean SLA within the -197cm mean DOT contour relative to the monthly mean SLA along the -190cm mean DOT contour. The Weddell Gyre depth is the monthly mean SLA within the -211cm mean DOT contour relative to the monthly mean SLA along the -205cm mean DOT contour (see map in Figure 6). This gyre depth metric is intended to capture the difference in sea level between the edge of the gyre and the gyre center, and hence reflects the variability of wind-driven surface divergence. The wind curl is calculated as $\nabla \times \left(|\underline{\boldsymbol{u}}_{\mathbf{10}}| \, \underline{\boldsymbol{u}}_{\mathbf{10}} \right)$ (after *Giles et al.* [2012]), where $\underline{\boldsymbol{u}}_{\mathbf{10}}$ is the ERA-Interim 10-m vector wind; over the Ross Gyre the gyre-mean wind curl is calculated within the -190cm DOT contour and over the Weddell Gyre the gyre-mean wind curl is calculated within the -205cm DOT contour. Finally, to avoid spurious correlation, we remove the seasonal cycle of gyre depth and wind curl. The choice to use wind curl rather than the wind stress curl as a surface atmospheric forcing metric was deliberate and intended to isolate the influence of wind variability in a region where the surface drag coefficient is heavily modified by the presence of sea ice in ways that may not be well-represented in reanalyses (e.g., [*Tsamados et al.*, 2014]). We have compared the wind curl from different reanalyses in the Ross and Weddell Gyre regions and conclude that there is a negligible effect on the correlation between the gyre depths and wind curl, and that our interpretation of the results is unaffected by the choice of reanalysis product (Figure S1; Tables S1 and S2).

3.2.1 Ross Gyre variability

Figure 4a & b show the mean dynamic topography and geostrophic circulation of the Ross Gyre region for 2011-2016. In the west, the Ross gyre is constrained by the intersection of the westernmost portion of the Pacific-Antarctic Ridge and the Balleny Fracture Zone. To the north both the Ross Gyre and the southern boundary of the ACC roughly follow the southern edge of the Pacific-Antarctic ridge to the northeast. The ACC then deflects to the east and south over the Udintsev Fracture Zone, one branch flowing south towards the Amundsen Sea and the other branch continuing to the east and the Antarctic Peninsula. Mean current speeds in the center of the Ross Gyre, a region of surface divergence, are generally lower than 0.5 cm/s. The Ross Gyre circulation can be split into at least two sub-gyres: the main, central Ross Gyre, and a secondary gyre circulation centered on the Balleny Islands, the Balleny Gyre, at the western limit of the Ross Gyre (Figure 4a & b). Seasonal sea level anomalies in the Ross Gyre region reveal a distinct seasonal cycle (Figure 4c). Coastal sea level is highest in autumn (AMJ) and is lowest in spring and summer (OND and JFM), while the SLA in the central gyre region shows a minimum in AMJ. This pattern of variability implies that the ASC, or at least its barotropic component, is strongest during AMJ and weaker during OND and JFM. Indeed, examining the SSH and current speed seasonal variations across the Southern Ocean reveals that ASC speeds are faster in AMJ (Figure 7b). Non-seasonal month-to-month variations in the depth of the Ross Gyre interior are significantly correlated with the wind curl (R = -0.58), affirming that the gyre is strongly influenced by the gyre-averaged wind forcing (Figure 6a).

3.2.2 Weddell Gyre variability

The Weddell gyre boundary closely follows the shelf break in the southern and western Weddell Sea: in the Riiser-Larsen and Lazarev Seas, the shelf is quite narrow, but in the Weddell Sea the ASC is deflected away from the coast by the wide shelves off the Filchner-Ronne Ice Shelf and the Eastern Antarctic Peninsula (Figure 5). There is a branch of the continental slope current system that flows across the continental shelf towards the Filchner-Ronne Ice Shelf, apparently following the Berkner Bank [*Darelius et al.*, 2016]. Unlike the Ross Gyre, the eastward-flowing northern portion of the Weddell Gyre is separated from the ACC by the South Sandwich Fracture Zone and the southern edge of the Southwest Indian Ridge [*Gordon*, 1981;

Heywood et al., 2004]. Along its eastern boundary, the Weddell gyre is not strongly constrained by bathymetric features, but broadly turns to the southwest, towards the Riiser-Larsen and Lazarev Seas. The Weddell Gyre shows a similar seasonal cycle to the Ross (Figure 5c): the westward-flowing ASC is strongest in AMJ and weakest in OND. However, the magnitude of the seasonal cycle is greater than in the Ross, with current speeds seasonally doubling in regions of the southern Weddell gyre sector (Figure 7b). The seasonal SLA climatology in the Weddell Gyre region (and to a lesser extent in the Ross gyre region) shows some north-south 'striping' artifacts, particularly visible in the AMJ and JAS composites (Figure 5c). These patterns are a result of the CS-2 orbital precession as it samples SSH during the course of a monthly orbital sub-cycle (the CS-2 orbit repeats only every 369 days with an approximately 30-day sub-cycle); as such, they constitute an error of commission, do not represent the mean state of the ocean and should not be interpreted as oceanographic signals. As with the Ross Gyre, the non-seasonal depth of the Weddell Gyre also shows good correlation with the non-seasonal wind curl (R = -0.67), again suggesting that the gyre-averaged wind forcing plays an important role in the gyre circulation variability (Figure 6b).

3.3 Response to climate forcing

3.3.1 Southern Oscillation

The SOI composites are dominated by a significantly correlated center of action in the Pacific sector, where positive (negative) SOI values are associated with negative (positive) SLA (Figure 8a-b). At the same time, the opposite is true in the Pacific sector of coastal Antarctica; here, positive (negative) SOI values are significantly correlated with positive (negative) SLA. This corresponds well with the wind forcing (Figure 8c-d): negative SLP anomalies in the South

Pacific, associated with positive phases of the SOI, are associated with cyclonic surface wind anomalies that tend to increase Ekman divergence, lowering sea level in the South Pacific, with the coastal divergence in the south resulting in drops in sea level. The opposite is true during negative SOI phases, with high SLP anomalies in the South Pacific giving rise to Ekman convergence and positive sea level anomalies in the Pacific sector of the ACC, whereas near the coast, enhanced onshore Ekman transport raises sea level. We find some persistence in the correlation between SLA and the SOI (Figure S6). This at least partially reflects the decorrelation time scale of the SOI, which shows significant autocorrelation for up to 9 months lag (Figure S8). However, it is difficult to draw conclusions about correlations at longer lags: while there will be an interior, baroclinic response of the gyres to surface wind forcing over longer timescales, the degree to which this isopycnal displacement will modify the SSH signature is not clear. An investigation into the interior response to the SOI that occurs in conjunction with the SSH response is an obvious future direction of study. What is clear is that the correlation is greatest at zero lag, and that we are observing the near-instantaneous, average barotropic response to the climate forcing in Figure 8a-b.

Between 2011-2016, there was a negative trend in the SOI associated with a shift from La Niña conditions in 2010-12 to the strong El Niño event of 2015-16. This is reflected by dropping sea levels in the Pacific sector of coastal Antarctica and rising sea levels in the South Pacific, anti-cyclonic current anomalies in the south Pacific and a weakening of the ASC, predominantly in the Ross, Amundsen and Bellingshausen Seas. *Boening et al.* [2011] reported on a record ocean bottom pressure measured by the GRACE satellites in late 2009 and early 2010 in this region of the South Pacific, which they linked to wind stress curl anomalies. Taken together, these results suggest that this extreme was likely linked to the phase of the Southern Oscillation, which was negative in late 2009-early 2010, and further, the results of *Boening et al.* [2011] suggest that this high frequency SSH signal is mostly wind-driven and barotropic in nature. We calculated the SLA during the peak of the 2015-16 El Niño, taken here to be June 2015 – April 2016 based on the sustained minimum of the SOI (Figure 10c). Indeed, there were positive sea level anomalies of 8-10cm in the South Pacific and negative sea level anomalies of up to -6cm in the Ross and Bellingshausen Seas (collectively known as the Amundsen Sea Sector, ASS).

3.3.2 Southern Annular Mode

The SLA is significantly correlated with the SAM over large regions of the Southern Ocean, and to leading order shows a zonally-symmetric mode of variability (Figure 9a-b). During positive SAM phases the trough in DOT surrounding Antarctica is deepened, and, vice versa, during negative phases the trough is flattened to an extent. This pattern of sea level variability is concurrent with contraction (expansion) of the belt of westerly winds surrounding Antarctic during positive (negative) SAM phases (Figure 9c-d). When the belt of westerlies contracts towards Antarctica northward Ekman transport is enhanced in the south, lowering sea level, and when the belt of westerlies expands northwards the opposite is true. As with the SOI, we find that the correlation between SLA and the SAM is greatest at zero lag, but that there is some persistence to the correlation (Figure S7). SLA is largely decorrelated from the SAM after 10 months, partially reflecting the quicker decorrelation time scale of the SAM index itself (Figure S8). It is clear that the near-instantaneous, average barotropic response to the SAM is being observed in Figure 9.

While the sea level response to the SAM is zonally symmetric to leading order, there are zonally asymmetric aspects. The wind anomalies associated with the SAM are strongest in the

South Indian and Southwest Pacific sectors. In the South Indian Ocean, there is a strong sea level response, with anticyclonic (cyclonic) wind anomalies driving positive (negative) SLA. This response is not perfectly opposing between the positive and negative SAM phases, with the cyclonic wind anomalies during negative SAM further east and more intense than the anticyclonic wind anomalies during positive SAM. This leads to large negative SLA in the South Indian Ocean that is not matched by the positive SLA during positive SAM. The regional extent of the negative and positive SLA surrounding Antarctica associated with the SAM corresponds very well with the southern boundary of the ACC as defined by [*Orsi et al.*, 1995] (Figure 9a & b).

Finally, *Langlais et al.* [2015] has shown that a full understanding of the response of the ACC and Antarctic margins circulation to climate variability requires looking at the phasing of both SAM and SOI, and in particular, wind stress perturbations over the core of the ACC or the Antarctic margins. The latter region supporting closed *f/H* (Coriolis frequency/depth, or approximately potential vorticity) contours will exhibit either predominantly baroclinic or barotropic responses as discussed by *Hughes et al.* [1999] and *Zika et al.* [2013]. A combination of both SSH and in situ data is needed to probe this question completely.

4 Discussion

4.1 Seasonal variability of the ASC

Section 3.2 examined the full seasonal SSH variability of the seasonally ice-covered Ross and Weddell gyres (Figures 4 & 5). There is a distinct seasonal cycle: coastal sea level peaks in Autumn (AMJ) and is a minimum in spring and summer (OND/JFM); away from the continental shelf the seasonal oscillation has the opposite phase with the 'seesaw' apparently pivoting over the shelf break. In fact, our data shows that this pattern of SSH seasonality is an almost circumpolar feature of coastal Antarctica, and leads to an ASC surface geostrophic flow that is strongest in AMJ and weakest in OND/JFM (Figure 7). This corroborates the modelled results of *Mathiot et al.* [2011], who found that the westward ASC transport peaks in June and is a minimum in December. They also found that the magnitude of the ASC seasonal cycle is greater in the Weddell Gyre region than the Ross Gyre region, and is smallest in the ASS, which is again supported by our results (Figure 7). *Mathiot et al.* [2011] found that the ASC mean flow and seasonal cycle is largely dominated by wind forcing: the coastal easterlies lead to Ekman convergence of fresh surface waters and coastal downwelling, reflected by increased SLA and westward geostrophic flow. The seasonal cycle of the coastal easterlies, strongest in autumn and weakest in spring, tends to enhance (reduce) Ekman convergence in autumn (spring) leading to the seasonal SSH variability shown in Figure 7a. The observed seasonal SSH variability agrees well in magnitude and spatial distribution with *Mathiot et al.* [2011] (their Figure 15), with seasonal SLA reaching ±5 cm.

There are few observational studies with which to compare our results. *Jacobs* [1991] summarized what was known of ASC current speeds at the time, reporting surface drift of ships and icebergs ranging between 4 and 15 cm/s, consistent with the satellite-derived geostrophic currents speeds of 2-10 cm/s. *Nunez-Riboni and Fahrbach* [2009] presented moored hydrographic results from the Weddell Sea and found that the seasonal cycle in ASC speed accounted for 37% of its variability with tides and other high frequency events accounting for most of the remaining variability. Their data showed that the zonal barotropic current speed roughly doubles seasonally at this location (the southern Weddell Gyre continental shelf at 0°E), peaking in AMJ. Our results are consistent with this, with current speeds varying seasonally from

3 to 6 cm/s at this location, peaking in AMJ (Figure 5c and 7b). They concluded that the seasonal cycle of the zonal wind accounts for 58% of the barotropic component of the ASC seasonal cycle, but they note that this is modulated by the transfer of momentum through a seasonally evolving sea ice pack. During the sea ice growth season the ice pack is highly mobile, particularly in the coastal regions and particularly in the Weddell gyre region [*Kwok et al.*, 2017], and the drag it exerts is at its annual maximum, which enhances the ASC [*Nunez-Riboni and Fahrbach*, 2009]. As ice growth continues in subsequent months, and the ice pack becomes more consolidated, sea ice drift is reduced and internal ice forces increase, damping the transfer of momentum from the atmosphere to the ocean [*Kwok et al.*, 2017], and contributing to a reduced ASC flow.

Finally, it is important to emphasize here that the SSH product that has been developed for this study has a spatial resolution on the order of 80-100 km, and that, therefore, our discussion of the ASC refers to the frontal system that occupies the continental slope surrounding Antarctica. Recent high-resolution modelling and observational studies have shown that the ASC is actually comprised of multiple frontal jets that may migrate across the slope [*Stern et al.*, 2015; *Peña-Molino et al.*, 2016; *Azaneu et al.*, 2017]. In agreement with the local deformation radius, these jets are often only a few tens of kilometers or smaller in scale, and they tend to be faster than the 2-10 cm/s inferred from the SSH data. This smaller-scale variability is not captured by our SSH product and the details of how the eddy circulation of the Antarctic shelf-slope system [*Thompson et al.*, 2014] responds to the seasonal cycle of the ASC shown here requires further study. This new SSH time series is potentially an important product for either future data assimilation activities or model validation.

4.2 Nonseasonal variability of the ASC

There are significant nonseasonal elements of variability in the ASC, of particular note are the coastal sea level anomalies (and strengthening/weakening of the ASC) associated with the Southern Oscillation and in particular the negative SLA and ASC weakening associated with the 2015-2016 El Niño event (Figures 8 & 10). Westerly along-shore wind anomalies observed during the 2015-2016 El Niño would tend to drive weaker on-shore Ekman transport, less coastal convergence and reduced downwelling (Figure 10b). The negative sea level anomalies in the ASS as well as the Ross, D'Urville, Mawson and Davis Seas during the 2015-2016 El Niño are consistent with this picture (Figure 10a), as reduced on-shore Ekman transport would lead to lower sea levels. Reduced downwelling could also lead to shoaling of isopycnal surfaces at depth, and while we cannot determine the subsurface response using the SSH data alone, there are various studies that link along-shore wind anomalies with the delivery of oceanic heat onto the continental shelves. There is evidence that the strength of the along-shore winds, and their associated impact on the density distribution with depth, modulates the delivery of warm Circumpolar Deep Water (CDW) to the continental shelf, both by shaping which density classes have access to the shelf and preconditioning for mesoscale eddy formation [*Nost et al.*, 2011; *Stewart and Thompson*, 2012; *St-Laurent et al.*, 2013; *Stewart and Thompson*, 2015]. This effect has been shown to be particularly relevant in the ASS, where it can influence bottom melting of the Pine Island Glacier (PIG) ice shelf [*Thoma et al.*, 2008]. *Dutrieux et al.* [2014] found that oceanic melting of the PIG ice shelf was reduced by around 50% during the 2010-12 La Niña due to anomalous easterly winds and increased coastal convergence that depressed isopycnal surfaces, reducing the depth of the CDW layer on the continental shelf. During El Niño conditions, it would be reasonable to expect the opposite to occur, with less coastal convergence (or a reversal) and raising of isopycnals leading to greater oceanic heat delivery to the PIG ice shelf cavity. However, *Webber et al.* [2017] linked the cold ocean conditions close to the PIG in 2012 to local surface heat fluxes, and suggested that ocean circulation variability plays a secondary role in forcing local ocean heat content variability.

Our data suggests that wind forcing associated with the Southern Oscillation does affect coastal sea level and the strength of the ASC over much of the Pacific sector of the Antarctic continental shelf. Negative SLA during the 2015-2016 El Niño could imply shoaling of isopycnal surfaces, however the ASC can be strongly barotropic [*Nunez-Riboni and Fahrbach*, 2009], so reduced DOT gradients could also correspond to a weakened barotropic flow with no baroclinic response. So, while we cannot conclude from our data alone whether there was increased oceanic heat delivery to the ASS continental shelf during this event, linking SSH variability to subsurface changes is an obvious future direction for study. *Spence et al.* [2014] found a link between the long-term positive trend in the SAM [*Marshall*, 2003] and increased ocean heat content at 200-700m depths surrounding Antarctica and weakening of the ASC. While our SLA dataset is too short to observe the impact of such long-term changes, the SAM SLA composites (Figure 9) clearly suggest that a long-term shift from negative to positive SAM and contraction of the westerly winds will act to weaken the ASC as waters in coastal Antarctic fall.

4.3 Ross and Weddell Gyre intensity

Our data suggests that month-to-month variations in the intensity of the Ross and Weddell Gyres are influenced to a large extent by the local wind curl in those regions (Figure 6). There are negative correlations between the non-seasonal Ross and Weddell Gyre wind curl and the non-seasonal SAM index (R = -0.40 ($p < 0.001$) and R = -0.41 ($p < 0.001$) respectively), suggesting that the strength of the gyre circulations is also modulated by the SAM. When the westerlies surrounding Antarctica contract, during positive SAM phases, they tend to strengthen the northern portions of the gyre circulations, leading to greater Ekman divergence, and an intensification of the gyre circulation, as reflected by increases in gyre depth. Long-term changes in the SAM [*Marshall*, 2003] might be expected to have opposing effects on the northern and southern portions of the Ross and Weddell Gyres: positive SAM values strengthen the northern portions of the gyres, promoting northward Ekman transport, whilst simultaneously weakening the ASC which constitutes the southern portion of the gyres. There is not a significant trend in the strength of the Ross or Weddell Gyres (at 95% confidence), which can likely be attributed to the relatively short time period and the large month-to-month variability in these relatively small oceanographic regions. The reported freshening trends in the Ross Gyre region [*Jacobs and Giulivi*, 2010] might be expected to produce a positive sea level trend, however these salinity trends are small relative to the time period covered by this study (0.03 psu decade^{-1}) and are derived from data collected on the continental shelf, so it is unclear how much this freshening signal would penetrate the interior Ross gyre given that this is a region of Ekman divergence.

5 Conclusions

SSH from CS-2 estimates in the seasonally ice-covered portion of the Southern Ocean have been combined with conventional CS-2 SSH estimates in the open ocean to produce monthly composites of DOT and SLA covering the entire Southern Ocean with monthly resolution between 2011-2016. This data reveals the full seasonal cycle of Southern Ocean sea level for the first time: coastal sea level peaks in autumn (AMJ) and is a minimum in spring and summer (OND & JFM). The pattern of seasonal sea level variability produces a seasonal cycle in the strength of the ASC, which peaks in autumn. The ASC is revealed to be an almost circumpolar feature, with mean current speeds in the range of 2-10 cm/s, but is generally strongest in eastern Antarctica, east of around 30°W, and is weakest in the ASS. The seasonal cycle of the ASC is largest in the Weddell Gyre region, particularly in the Lazarev, Riiser-Larsen and Cosmonaut Seas. This pattern of ASC seasonal variability agrees well with high-resolution modelled results [*Mathiot et al.*, 2011] as well as in situ observational data in the Weddell Gyre region [*Nunez-Riboni and Fahrbach*, 2009], with ASC speeds up to twice as fast in autumn. Month-to-month variability in the strength of the Ross and Weddell Gyre circulation is well correlated with local wind forcing, which in turn are weakly correlated with the SAM index. During positive SAM phases, as the westerlies surrounding Antarctic contract and strengthen, they enhance circulation in the northern portions of the Gyres, increasing Ekman divergence in the gyre centers, strengthening the gyre circulation.

The SAM and Southern Oscillation drive significant wind-forced sea level variability across the whole Southern Ocean including the marginal seas of Antarctica. The SAM produces a sea level response that is zonal to first order: during positive (negative) SAM phases the belt of westerlies surrounding Antarctica contracts (expands) and strengthens (weakens), and the DOT trough surrounding Antarctica is deepened (flattened), strengthening (weakening) the ACC. The Southern Oscillation sea level response is dominated by a center of action in the Pacific sector, where positive (negative) SOI values are associated with negative (positive) SLA. In the Pacific sector of coastal Antarctica, positive (negative) SOI values are significantly correlated with positive (negative) SLA, which correspond to a strengthening (weakening) of the ASC. During the peak of the 2015-2016 El Niño the ASC was weakened in the Pacific and Indian sectors.

The seasonally or perennially ice-covered regions of the Southern Ocean, such as the Antarctic continental shelves and the Ross and Weddell Gyres, are climatically important regions of water mass modification, surface heat freshwater and momentum fluxes, sea ice formation and terrestrial ice input. Thus, we anticipate that this new merged sea level record will be of significant interest to the Southern Ocean physical oceanography and glaciology communities, where studies of ocean variability and ocean-ice interactions have been limited by a lack of observations.

Acknowledgments

This work was carried out at the Jet Propulsion Laboratory and the California Institute of Technology under a contract with the National Aeronautics and Space Administration and funded through the President's and Director's Fund Program. CryoSat-2 data were supplied by the European Space Agency (https://earth.esa.int/web/guest/data-access). The Southern Ocean sea level data presented in this manuscript will be made available via https://rkwok.jpl.nasa.gov/cryosat/.

References

Armitage, T. W. K., S. Bacon, A. L. Ridout, A. A. Petty, S. Wolbach, and M. Tsamados (2017), Arctic Ocean surface geostrophic circulation 2003–2014, *The Cryosphere*, *11*(4), 1767-1780, doi:10.5194/tc-11-1767-2017.

Armitage, T. W. K., S. Bacon, A. L. Ridout, S. F. Thomas, Y. Aksenov, and D. J. Wingham (2016), Arctic sea surface height variability and change from satellite radar altimetry and GRACE, 2003-2014, *J Geophys Res-Oceans*, *121*(6), 4303-4322, doi:10.1002/2015jc011579.

Azaneu, M. V. C., K. J. Heywood, B. Y. Queste, and A. F. Thompson (2017), Variability of the Antarctic Slope Front in the northwestern Weddell Sea, *Journal of Physical Oceanography (in revsion)*.

Boening, C., T. Lee, and V. Zlotnicki (2011), A record-high ocean bottom pressure in the South Pacific observed by GRACE, *Geophys Res Lett*, *38*, doi:Artn L04602 10.1029/2010gl046013.

Bulczak, A. I., S. Bacon, A. C. N. Garabato, A. Ridout, M. J. P. Sonnewald, and S. W. Laxon (2015), Seasonal variability of sea surface height in the coastal waters and deep basins of the Nordic Seas, *Geophys Res Lett*, *42*(1), 113-120, doi:10.1002/2014gl061796.

Cazenave, A., H.-B. Dieng, B. Meyssignac, K. von Schuckmann, B. Decharme, and E. Berthier (2014), The rate of sea-level rise, *Nature Clim. Change*, *4*(5), 358-361, doi:10.1038/nclimate2159 http://www.nature.com/nclimate/journal/v4/n5/abs/nclimate2159.html - supplementary-information.

Cunningham, S. A., S. G. Alderson, B. A. King, and M. A. Brandon (2003), Transport and variability of the Antarctic Circumpolar Current in Drake Passage, *Journal of Geophysical Research: Oceans*, *108*(C5), n/a-n/a, doi:10.1029/2001JC001147.

Darelius, E., I. Fer, and K. W. Nicholls (2016), Observed vulnerability of Filchner-Ronne Ice Shelf to wind-driven inflow of warm deep water, *7*, 12300, doi:10.1038/ncomms12300 https://www.nature.com/articles/ncomms12300 - supplementary-information.

Dee, D. P., et al. (2011), The ERA-Interim reanalysis: configuration and performance of the data assimilation system, *Q J Roy Meteor Soc*, *137*(656), 553-597, doi:10.1002/qj.828.

Donohue, K. A., K. L. Tracey, D. R. Watts, M. P. Chidichimo, and T. K. Chereskin (2016), Mean Antarctic Circumpolar Current transport measured in Drake Passage, *Geophys Res Lett*, *43*(22), 11,760-711,767, doi:10.1002/2016GL070319.

Dutrieux, P., J. De Rydt, A. Jenkins, P. R. Holland, H. K. Ha, S. H. Lee, E. J. Steig, Q. H. Ding, E. P. Abrahamsen, and M. Schroder (2014), Strong Sensitivity of Pine Island Ice-Shelf Melting to Climatic Variability, *Science*, *343*(6167), 174-178, doi:10.1126/science.1244341.

Farrell, S. L., D. C. McAdoo, S. W. Laxon, H. J. Zwally, D. H. Yi, A. Ridout, and K. Giles (2012), Mean dynamic topography of the Arctic Ocean, *Geophys Res Lett*, *39*, doi:Artn L01601 10.1029/2011gl050052.

Fecher, T., R. Pail, T. Gruber, and G. Consortium (2017), GOCO05c: A New Combined Gravity Field Model Based on Full Normal Equations and Regionally Varying Weighting, *Surv Geophys*, *38*(3), 571-590, doi:10.1007/s10712-016-9406-y.

Fetterer, F., K. Knowles, W. Meier, M. Savoie, and A. K. Windnagel (2016), Sea ice Index, Version 2, edited, NSIDC: National Snow and Ice Data Center, Boulder, Colorado USA, doi:10.7265/N5736NV7.

Giles, K. A., S. W. Laxon, A. L. Ridout, D. J. Wingham, and S. Bacon (2012), Western Arctic Ocean freshwater storage increased by wind-driven spin-up of the Beaufort Gyre, *Nat Geosci*, *5*(3), 194-197, doi:10.1038/Ngeo1379.

Gill, A. E. (1973), Circulation and Bottom Water Production in Weddell Sea, *Deep-Sea Research*, *20*(2), 111-140, doi:Doi 10.1016/0011-7471(73)90048-X.

Goddard, P. B., C. O. Dufour, J. Yin, S. M. Griffies, and M. Winton (2017), CO2-Induced Ocean Warming of the Antarctic Continental Shelf in an Eddying Global Climate Model, *Journal of Geophysical Research: Oceans*, *122*(10), 8079-8101, doi:10.1002/2017JC012849.

Gordon, A. L. (1981), South-Atlantic Thermocline Ventilation, *Deep-Sea Res*, *28*(11), 1239-1264, doi:Doi 10.1016/0198-0149(81)90033-9.

Heywood, K. J., A. C. N. Garabato, D. P. Stevens, and R. D. Muench (2004), On the fate of the Antarctic Slope Front and the origin of the Weddell Front, *J Geophys Res-Oceans*, *109*(C6), doi:Artn C06021
10.1029/2003jc002053.

Hogg, A. M. (2010), An Antarctic Circumpolar Current driven by surface buoyancy forcing, *Geophys Res Lett*, *37*, doi:Artn L23601
10.1029/2010gl044777.

Hughes, C. W., M. P. Meredith, and K. J. Heywood (1999), Wind-driven transport fluctuations through drake passage: A southern mode, *J Phys Oceanogr*, *29*(8), 1971-1992, doi:Doi 10.1175/1520-0485(1999)029<1971:Wdtftd>2.0.Co;2.

Jacobs, S. S. (1991), On the Nature and Significance of the Antarctic Slope Front, *Mar Chem*, *35*(1-4), 9-24.

Jacobs, S. S., and C. F. Giulivi (2010), Large Multidecadal Salinity Trends near the Pacific-Antarctic Continental Margin, *J Climate*, *23*(17), 4508-4524, doi:10.1175/2010jcli3284.1.

Jones, C. S., and P. Cessi (2016), Interbasin Transport of the Meridional Overturning Circulation, *J Phys Oceanogr*, *46*(4), 1157-1169, doi:10.1175/Jpo-D-15-0197.1.

Kim, Y. S., and A. H. Orsi (2014), On the Variability of Antarctic Circumpolar Current Fronts Inferred from 1992-2011 Altimetry, *J Phys Oceanogr*, *44*(12), 3054-3071, doi:10.1175/Jpo-D-13-0217.1.

Kwok, R., and J. Morison (2011), Dynamic topography of the ice-covered Arctic Ocean from ICESat, *Geophys Res Lett*, *38*, doi:Artn L02501
10.1029/2010gl046063.

Kwok, R., and J. Morison (2016), Sea surface height and dynamic topography of the ice-covered oceans from CryoSat-2: 2011-2014, *J Geophys Res-Oceans*, *121*(1), 674-692, doi:10.1002/2015jc011357.

Kwok, R., S. S. Pang, and S. Kacimi (2017), Sea ice drift in the Southern Ocean: Regional patterns, variability, and trends, *Elementa Science of the Anthropocene*, *5*, 32, doi:10.1525/elementa.226.

Langlais, C. E., S. R. Rintoul, and J. D. Zika (2015), Sensitivity of Antarctic Circumpolar Current Transport and Eddy Activity to Wind Patterns in the Southern Ocean, *J Phys Oceanogr*, *45*(4), 1051-1067, doi:10.1175/Jpo-D-14-0053.1.

Laxon, S. (1994), Sea-Ice Altimeter Processing Scheme at the Eodc, *Int J Remote Sens*, *15*(4), 915-924.

Laxon, S., and D. Mcadoo (1994), Arctic-Ocean Gravity-Field Derived from Ers-1 Satellite Altimetry, *Science*, *265*(5172), 621-624, doi:DOI 10.1126/science.265.5172.621.

Lumpkin, R., and K. Speer (2007), Global ocean meridional overturning, *J Phys Oceanogr*, *37*(10), 2550-2562, doi:10.1175/Jpo3130.1.

Marshall, G. J. (2003), Trends in the southern annular mode from observations and reanalyses, *J Climate*, *16*(24), 4134-4143, doi:Doi 10.1175/1520-0442(2003)016<4134:Titsam>2.0.Co;2.

Mathiot, P., H. Goosse, T. Fichefet, B. Barnier, and H. Gallée (2011), Modelling the seasonal variability of the Antarctic Slope Current, *Ocean Sci.*, *7*(4), 455-470, doi:10.5194/os-7-455-2011.

Mizobata, K., E. Watanabe, and N. Kimura (2016), Wintertime variability of the Beaufort gyre in the Arctic Ocean derived from CryoSat-2/SIRAL observations, *J Geophys Res-Oceans*, *121*(3), 1685-1699, doi:10.1002/2015jc011218.

Nost, O. A., M. Biuw, V. Tverberg, C. Lydersen, T. Hattermann, Q. Zhou, L. H. Smedsrud, and K. M. Kovacs (2011), Eddy overturning of the Antarctic Slope Front controls glacial melting in the Eastern Weddell Sea, *J Geophys Res-Oceans*, *116*, doi:Artn C11014 10.1029/2011jc006965.

Nunez-Riboni, I., and E. Fahrbach (2009), Seasonal variability of the Antarctic Coastal Current and its driving mechanisms in the Weddell Sea, *Deep-Sea Res Pt I*, *56*(11), 1927-1941, doi:10.1016/j.dsr.2009.06.005.

Orsi, A. H., T. Whitworth, and W. D. Nowlin (1995), On the Meridional Extent and Fronts of the Antarctic Circumpolar Current, *Deep-Sea Res Pt I*, *42*(5), 641-673, doi:Doi 10.1016/0967-0637(95)00021-W.

Pail, R., et al. (2010), Combined satellite gravity field model GOCO01S derived from GOCE and GRACE, *Geophys Res Lett*, *37*, doi:Artn L20314

10.1029/2010gl044906.

Pavlis, N. K., S. A. Holmes, S. C. Kenyon, and J. K. Factor (2013), The Development and Evaluation of the Earth Gravitational Model 2008 (EGM2008), *J Geophys Res-Sol Ea*, *118*(5), 2633-2633, doi:10.1002/jgrb.50167.

Peacock, N. R., and S. W. Laxon (2004), Sea surface height determination in the Arctic Ocean from ERS altimetry, *J Geophys Res-Oceans*, *109*(C7), doi:Artn C07001
10.1029/2001jc001026.

Peña-Molino, B., M. S. McCartney, and S. R. Rintoul (2016), Direct observations of the Antarctic Slope Current transport at 113°E, *Journal of Geophysical Research: Oceans*, *121*(10), 7390-7407, doi:10.1002/2015JC011594.

Pope, J. O., P. R. Holland, A. Orr, G. J. Marshall, and T. Phillips (2017), The impacts of El Niño on the observed sea ice budget of West Antarctica, *Geophys Res Lett*, n/a-n/a, doi:10.1002/2017GL073414.

Rye, C. D., A. C. N. Garabato, P. R. Holland, M. P. Meredith, A. J. G. Nurser, C. W. Hughes, A. C. Coward, and D. J. Webb (2014), Rapid sea-level rise along the Antarctic margins in response to increased glacial discharge, *Nat Geosci*, *7*(10), 732-735, doi:10.1038/Ngeo2230.

Scagliola, M., and M. Fornari (2017), Known biases in CryoSat Level1b products, *ESA Technical Note: C2-TN-ARS-GS-5135*.

Scharroo, R., E. W. Leuliette, J. L. Lillibridge, D. Byrne, M. C. Naeije, and G. T. Mitchum (2013a), RADS: Consistent multi-mission products, *Proceedings of the Symposium on 20 Years of Progress in Radar Altimetry, Venice, 20-28 September 2012, ESA SP-710*.

Scharroo, R., W. H. F. Smith, E. W. Leuliette, and J. L. Lillibridge (2013b), The performance of CryoSat-2 as an ocean altimeter, *Proceedings of the CryoSat-2 Third User Workshop, Dresden, 12-14 March 2013, ESA SP-717*.

Schmidtko, S., K. J. Heywood, A. F. Thompson, and S. Aoki (2014), Multidecadal warming of Antarctic waters, *Science*, *346*(6214), 1227-1231, doi:10.1126/science.1256117.

Snyder, J. P. (1987), Map Projections - A Working Manual, *U.S. Geological Survey Professional Paper 1395, U.S. Government Printing Office, Washington D.C.*, pp. 154-163.

Sokolov, S., and S. R. Rintoul (2009), Circumpolar structure and distribution of the Antarctic Circumpolar Current fronts: 2. Variability and relationship to sea surface height, *J Geophys Res-Oceans*, *114*, doi:Artn C11019
10.1029/2008jc005248.

Spence, P., S. M. Griffies, M. H. England, A. M. Hogg, O. A. Saenko, and N. C. Jourdain (2014), Rapid subsurface warming and circulation changes of Antarctic coastal waters by poleward shifting winds, *Geophys Res Lett*, *41*(13), 4601-4610, doi:10.1002/2014gl060613.

Spence, P., R. M. Holmes, A. M. Hogg, S. M. Griffies, K. D. Stewart, and M. H. England (2017), Localized rapid warming of West Antarctic subsurface waters by remote winds, *Nat Clim Change*, *7*(8), 595-603, doi:10.1038/Nclimate3335.

St-Laurent, P., J. M. Klinck, and M. S. Dinniman (2013), On the Role of Coastal Troughs in the Circulation of Warm Circumpolar Deep Water on Antarctic Shelves, *J Phys Oceanogr*, *43*(1), 51-64, doi:10.1175/jpo-d-11-0237.1.

Stern, A., L.-P. Nadeau, and D. Holland (2015), Instability and Mixing of Zonal Jets along an Idealized Continental Shelf Break, *J Phys Oceanogr*, *45*(9), 2315-2338, doi:10.1175/jpo-d-14-0213.1.

Stewart, A. L., and A. F. Thompson (2012), Sensitivity of the ocean's deep overturning circulation to easterly Antarctic winds, *Geophys Res Lett*, *39*, doi:Artn L18604
10.1029/2012gl053099.

Stewart, A. L., and A. F. Thompson (2015), Eddy-mediated transport of warm Circumpolar Deep Water across the Antarctic Shelf Break, *Geophys Res Lett*, *42*(2), 432-440, doi:10.1002/2014gl062281.

Talley, L. D. (2013), Closure of the Global Overturning Circulation Through the Indian, Pacific, and Southern Oceans: Schematics and Transports, *Oceanography*, *26*(1), 80-97.

Thoma, M., A. Jenkins, D. Holland, and S. Jacobs (2008), Modelling Circumpolar Deep Water intrusions on the Amundsen Sea continental shelf, Antarctica, *Geophys Res Lett*, *35*(18), doi:Artn L18602
10.1029/2008gl034939.

Thompson, A. F., K. J. Heywood, S. Schmidtko, and A. L. Stewart (2014), Eddy transport as a key component of the Antarctic overturning circulation, *Nature Geosci*, *7*(12), 879-884, doi:10.1038/ngeo2289
http://www.nature.com/ngeo/journal/v7/n12/abs/ngeo2289.html - supplementary-information.

Thompson, A. F., A. L. Stewart, and T. Bischoff (2016), A Multibasin Residual-Mean Model for the Global Overturning Circulation, *J Phys Oceanogr*, *46*(9), 2583-2604, doi:10.1175/Jpo-D-15-0204.1.

Thompson, D. W. J., and J. M. Wallace (2000), Annular modes in the extratropical circulation. Part I: Month-to-month variability, *J Climate*, *13*(5), 1000-1016, doi:Doi 10.1175/1520-0442(2000)013<1000:Amitec>2.0.Co;2.

Tsamados, M., D. L. Feltham, D. Schroeder, D. Flocco, S. L. Farrell, N. Kurtz, S. W. Laxon, and S. Bacon (2014), Impact of Variable Atmospheric and Oceanic Form Drag on Simulations of Arctic Sea Ice*, *J Phys Oceanogr*, *44*(5), 1329-1353, doi:10.1175/Jpo-D-13-0215.1.

Turner, J., T. Phillips, G. J. Marshall, J. S. Hosking, J. O. Pope, T. J. Bracegirdle, and P. Deb (2017), Unprecedented springtime retreat of Antarctic sea ice in 2016, *Geophys Res Lett*, n/a-n/a, doi:10.1002/2017GL073656.

Webber, B. G. M., K. J. Heywood, D. P. Stevens, P. Dutrieux, E. P. Abrahamsen, A. Jenkins, S. S. Jacobs, H. K. Ha, S. H. Lee, and T. W. Kim (2017), Mechanisms driving variability in the ocean forcing of Pine Island Glacier, *Nat Commun*, *8*, doi:ARTN 14507 10.1038/ncomms14507.

Wessel, P., W. H. F. Smith, R. Scharroo, J. Luis, and F. Wobbe (2017), GMT Man Pages Release 5.3.3, *Available via* http://gmt.soest.hawaii.edu/projects/gmt/wiki/Documentation, *"nearneighbor" & "grdfilter"*.

Wingham, D. J., et al. (2006), CryoSat: A mission to determine the fluctuations in Earth's land and marine ice fields, *Adv Space Res-Series*, *37*(4), 841-871, doi:10.1016/j.asr.2005.07.027.

Zika, J. D., et al. (2013), Vertical Eddy Fluxes in the Southern Ocean, *J Phys Oceanogr*, *43*(5), 941-955, doi:10.1175/Jpo-D-12-0178.1.

Figure 1. Bathymetric map of the Southern Ocean, adjacent oceans and marginal seas. The floating ice shelves of the Antarctic ice sheets are shown in white bounded by thick black lines, while grounded ice (and other land areas) is shown in dark gray. The mean 15% September sea ice concentration contour is shown in yellow. Circulation features are shown in orange, including the Antarctic Circumpolar Current (ACC, the thickest orange arrows), the Antarctic Slope Current (ASC, parallel to the continental shelf), and the Ross, Weddell and Balleny Gyres (BG). Abbreviations used on the map are SST: South Sandwich Trench; SSFZ: South Sandwich

Fracture Zone; STR: South Tasman Rise; F-R Ice Shelf: Filchner-Ronne Ice Shelf; BB: Berkner Bank.

Figure 2. Data availability (given in number of months) during the period 2011-2016 from **a)** Radar Altimeter Database System (RADS) ice-free CryoSat-2 (CS-2) pulse-limited and SAR mode radar altimetry and **b)** the ice-covered plus ice-free composites. Regions of the open ocean with less the 72 months of coverage correspond to regions where CS-2 was operated in SAR-Interferometric mode for a portion of the mission.

Figure 3. a) The CS-2 2011-2016 mean dynamic topography estimated relative to the GOCO05c geoid (cm) with contours drawn every 10cm; **b)** the mean current speed (cm/s); **c)** the difference between the GOCO05c and EGM2008 geoid models (cm) for the Weddell Sea region (the black box in **(b)**); **d)** the GOCO05c and **e)** the EGM2008 current speed (cm/s) in the Weddell Sea region.

Figure 4. Seasonal variability of the Ross gyre: **a)** the mean dynamic ocean topography (cm, the color scale is purposefully saturated to highlight the Ross gyre); **b)** the geostrophic currents (cm/s); **c)** seasonal (January-March (JFM), April-June (AMJ), July-September (JAS), October-November (OND)) sea level anomaly composites (cm). The thick black line is the 1km isobath.

Figure 5. As in Figure 4, but for the Weddell gyre. Note the different color scales.

Figure 6. The non-seasonal gyre depth (cm, gray) and non-seasonal wind curl (10^{-5} m s^{-2}, orange) for the **a)** Ross and **b)** Weddell Gyres. Gyre depth is calculated as the mean SLA in the light blue shaded region minus the mean SLA along the dark blue contour. The wind curl is

calculated as the mean within the dark blue contour. Note that the axes are reversed for the wind curl.

Figure 7. a) The sea level difference (cm) and **b)** the change in current speed (%) between autumn (AMJ) and spring (OND). The missing data and increased spatial variability adjacent to the western Antarctic Peninsula reflects the poor data coverage in this region (Figure 2).

Figure 8. Composites of SLA (cm) for positive **(a)** and negative **(b)** SOI. The number of months is shown in brackets and the black contour contains regions where the SLA is significantly correlated with the SOI at the $p < 0.05$ level. Composites of surface atmospheric conditions for positive **(c)** and negative **(d)** SOI. Contours show sea level pressure every 1 mbar, solid contours positive, dashed contours negative, and vectors are the 10-m wind.

Figure 9. As in Figure 8, for the Southern Annular Mode. Shown in yellow in **(a)** and **(b)** is the southern boundary of the ACC as defined by *Orsi et al.* [1995].

Figure 10. June 2015-April 2016 time-mean sea level anomaly (cm) **(a)** and surface atmospheric circulation anomaly (m s^{-1}) **(b)** associated with the peak of the 2015-2016 El Niño event – the gray shaded period in **(c)**. The contours in **(b)** are drawn every 1 mbar and are solid (dashed) for positive (negative) pressure anomalies; vectors are the 10-m wind anomaly.

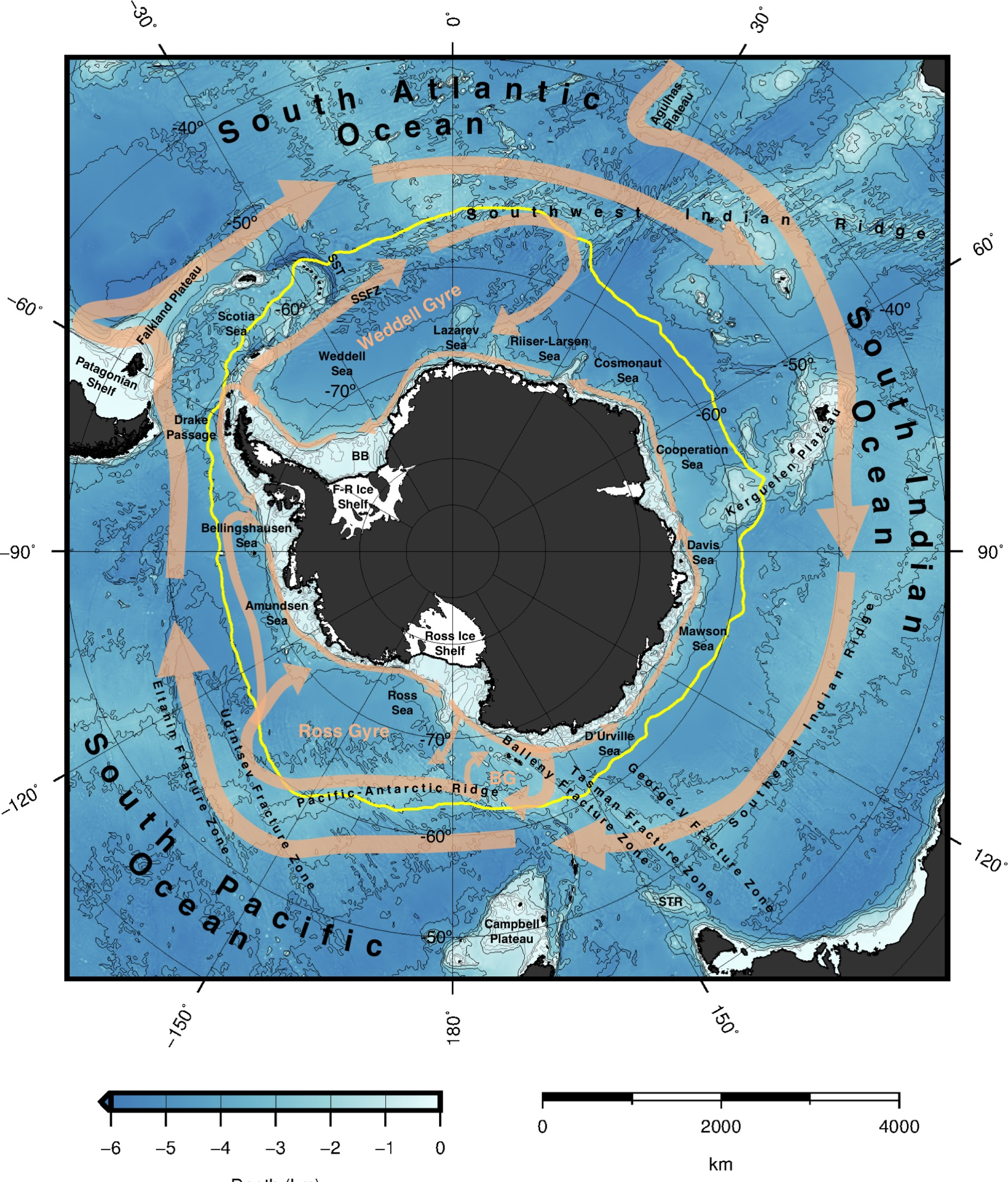
South Atlantic Ocean
South Indian Ocean
South Pacific Ocean
Southwest Indian Ridge
Agulhas Plateau
Falkland Plateau
Patagonian Shelf
Scotia Sea
SST
SSFZ
Weddell Gyre
Weddell Sea
Lazarev Sea
Riiser-Larsen Sea
Cosmonaut Sea
Cooperation Sea
Kerguelen Plateau
Drake Passage
BB
F-R Ice Shelf
Bellingshausen Sea
Amundsen Sea
Ross Ice Shelf
Ross Sea
Ross Gyre
BG
Davis Sea
Mawson Sea
D'Urville Sea
Balleny Fracture Zone
Tasman Fracture Zone
George V Fracture Zone
Southeast Indian Ridge
Eltanin Fracture Zone
Udintsev Fracture Zone
Pacific-Antarctic Ridge
STR
Campbell Plateau
-30°
0°
30°
60°
90°
120°
150°
180°
-150°
-120°
-90°
-60°
-40°
-50°
-60°
-70°
Depth (km)
−6
−5
−4
−3
−2
−1
0
2000
4000
km

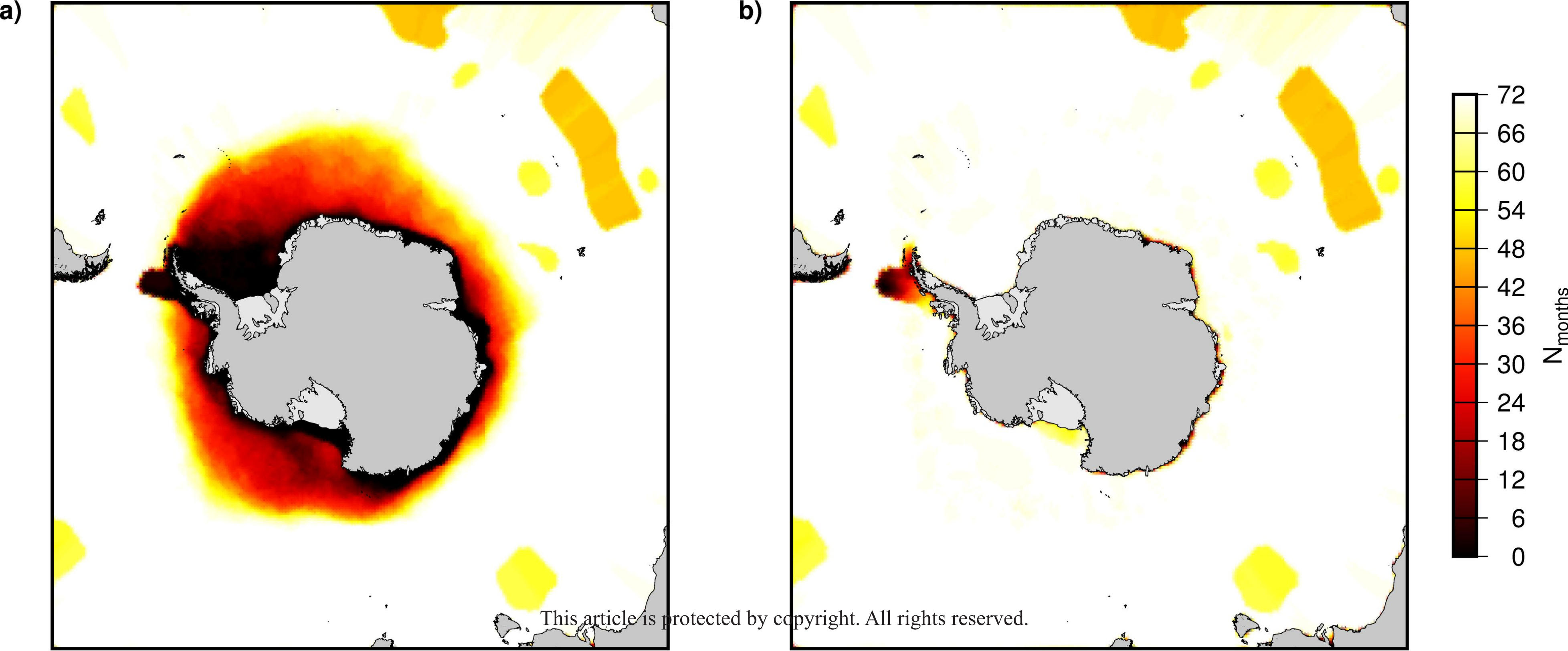

a)
b)
72
66
60
54
48
42
36
30
24
18
12
6
0
N_{months}

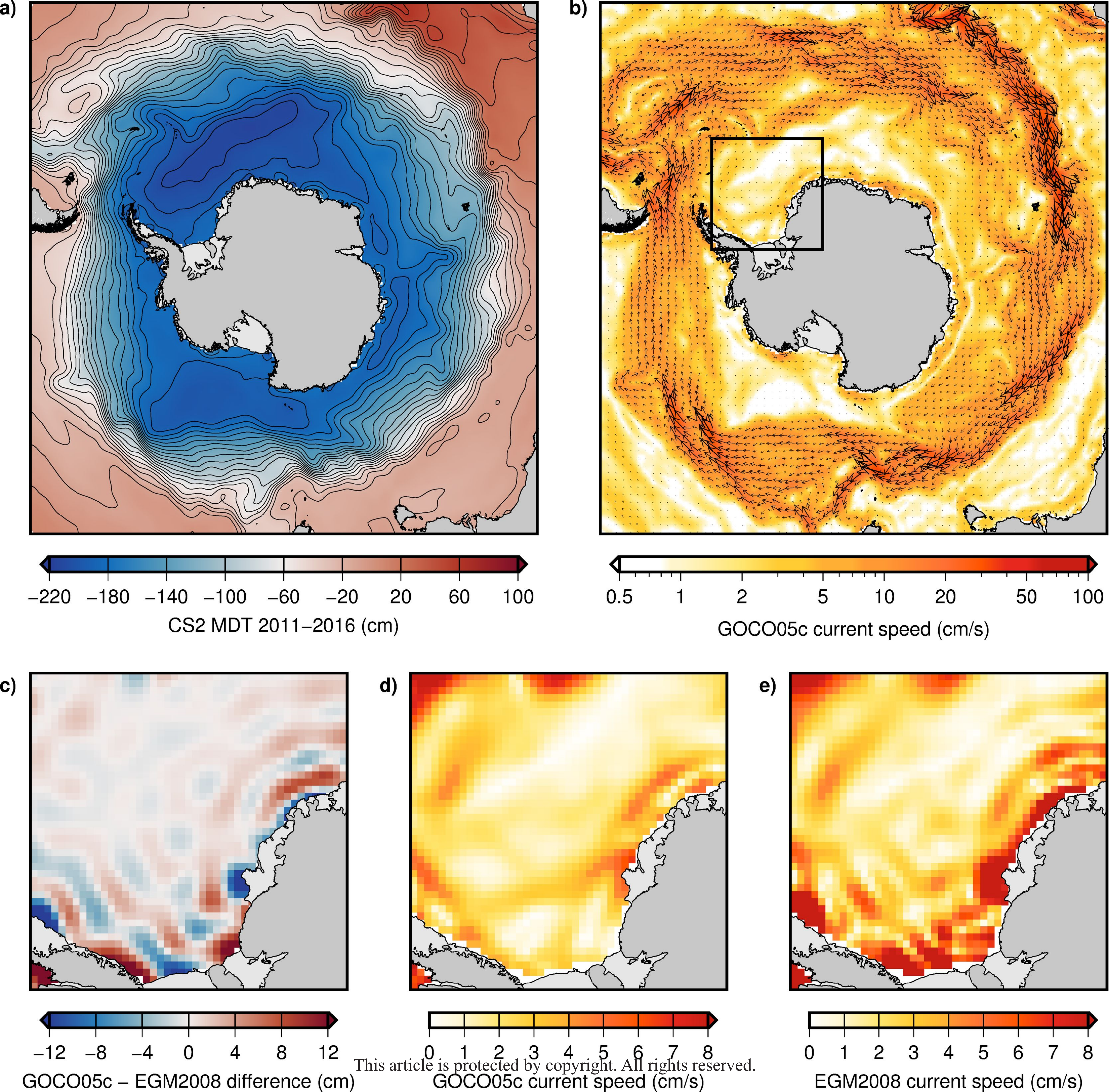
a)
b)
−220 −180 −140 −100 −60 −20 20 60 100
CS2 MDT 2011−2016 (cm)
0.5 1 2 5 10 20 50 100
GOCO05c current speed (cm/s)
c)
d)
e)
−12 −8 −4 0 4 8 12
GOCO05c − EGM2008 difference (cm)
0 1 2 3 4 5 6 7 8
GOCO05c current speed (cm/s)
0 1 2 3 4 5 6 7 8
EGM2008 current speed (cm/s)

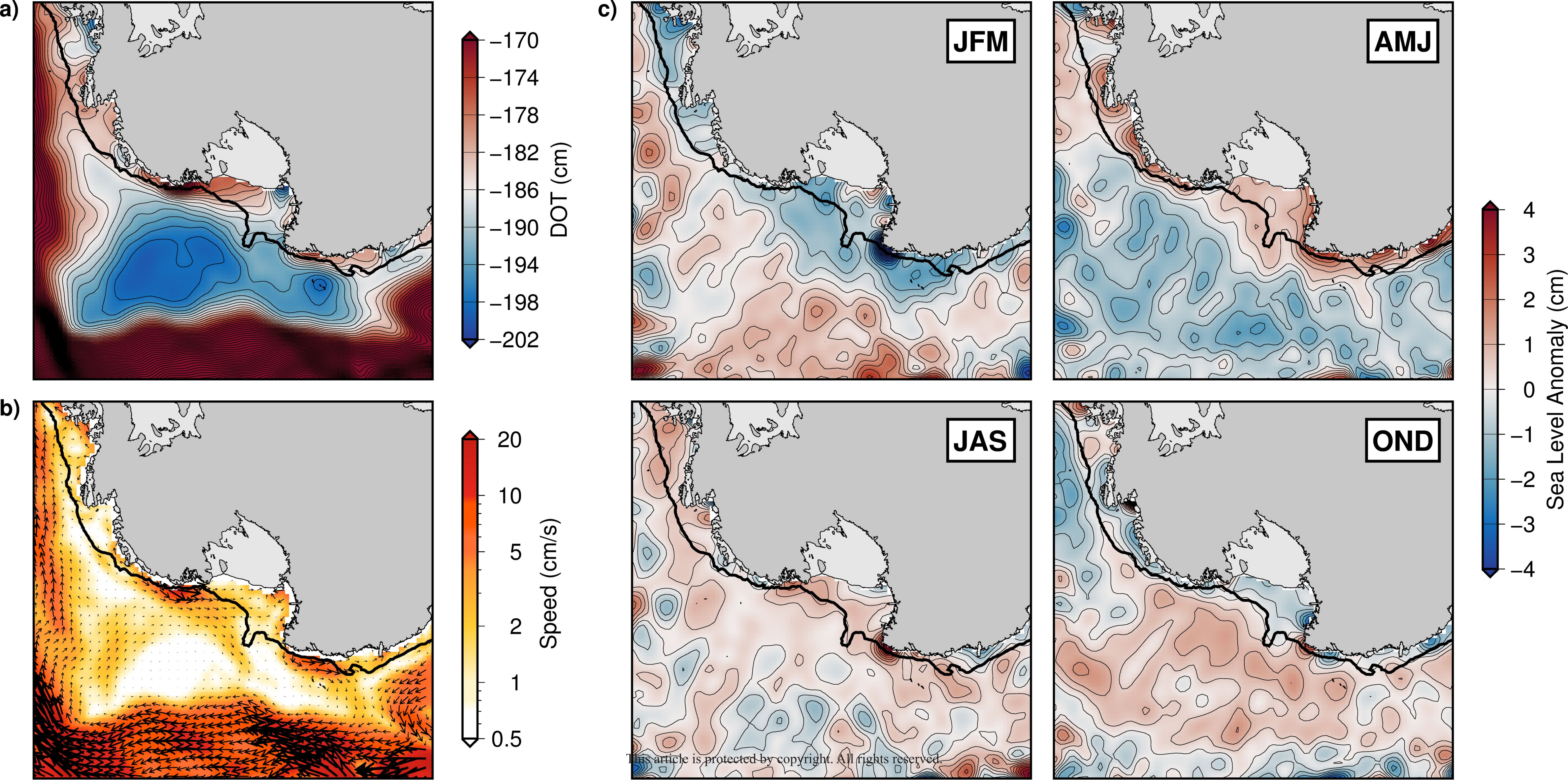

a)
b)
c)
JFM
AMJ
JAS
OND
−170
−174
−178
−182
−186
−190
−194
−198
−202
DOT (cm)
20
10
5
2
1
0.5
Speed (cm/s)
4
3
2
1
0
−1
−2
−3
−4
Sea Level Anomaly (cm)

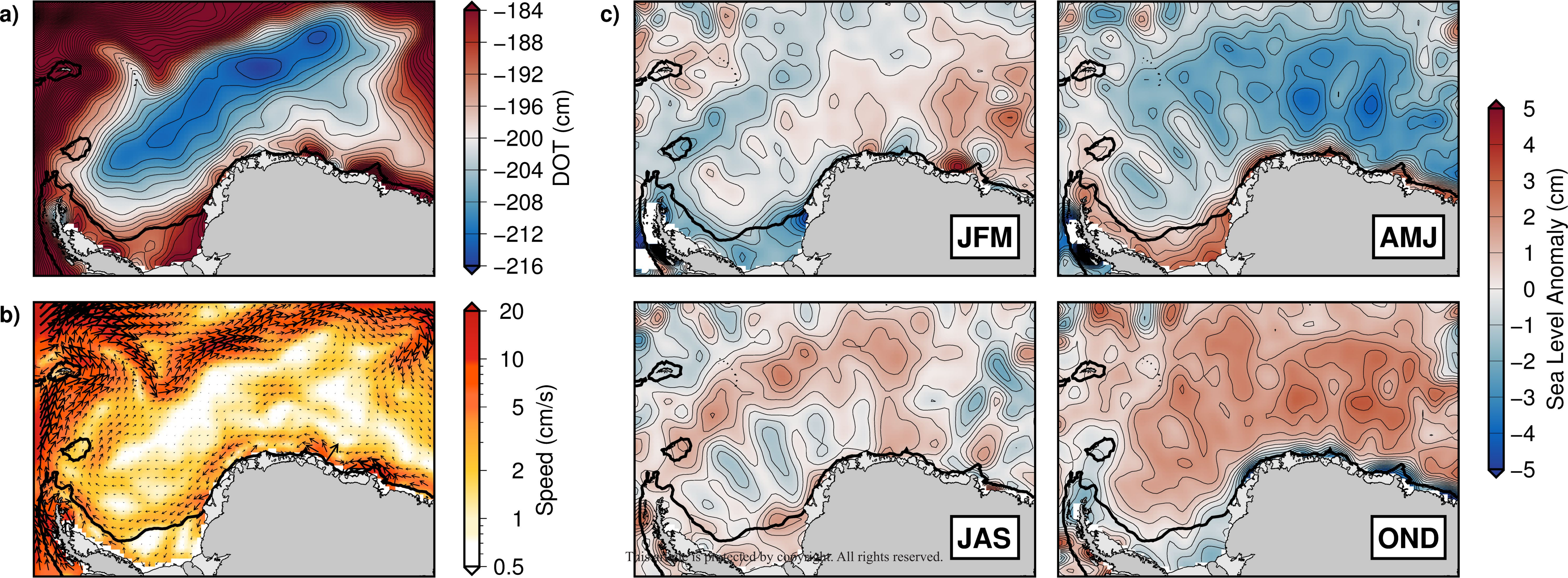
a)
−184
−188
−192
−196
−200
−204
−208
−212
−216
DOT (cm)
b)
20
10
5
2
1
0.5
Speed (cm/s)
c)
JFM
AMJ
JAS
OND
5
4
3
2
1
0
−1
−2
−3
−4
−5
Sea Level Anomaly (cm)

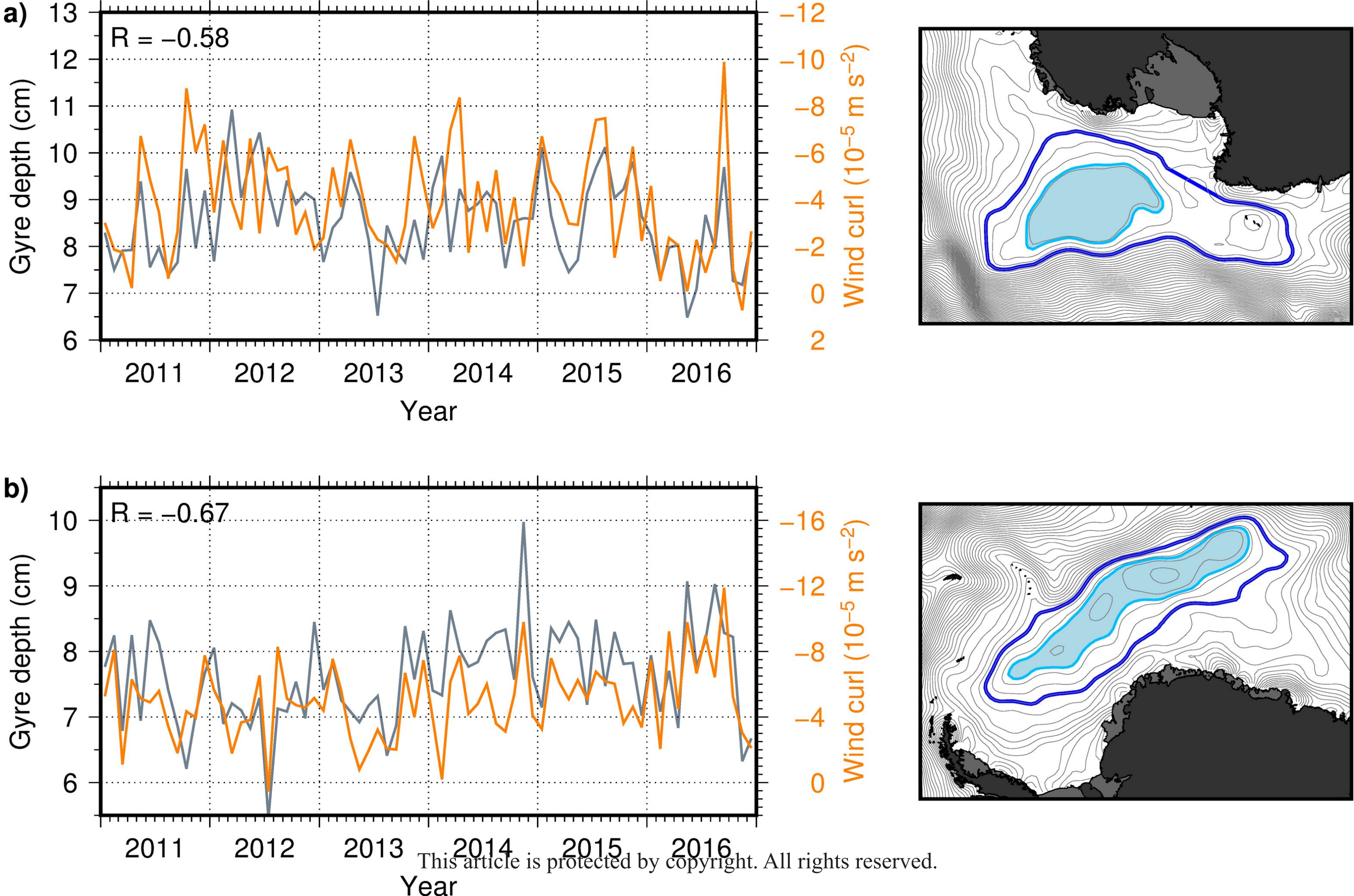
a)
R = −0.58
Gyre depth (cm)
Wind curl (10^{-5} m s^{-2})
13
12
11
10
9
8
7
6
−12
−10
−8
−6
−4
−2
0
2
2011
2012
2013
2014
2015
2016
Year
b)
R = −0.67
Gyre depth (cm)
Wind curl (10^{-5} m s^{-2})
10
9
8
7
6
−16
−12
−8
−4
0
2011
2012
2013
2014
2015
2016
Year

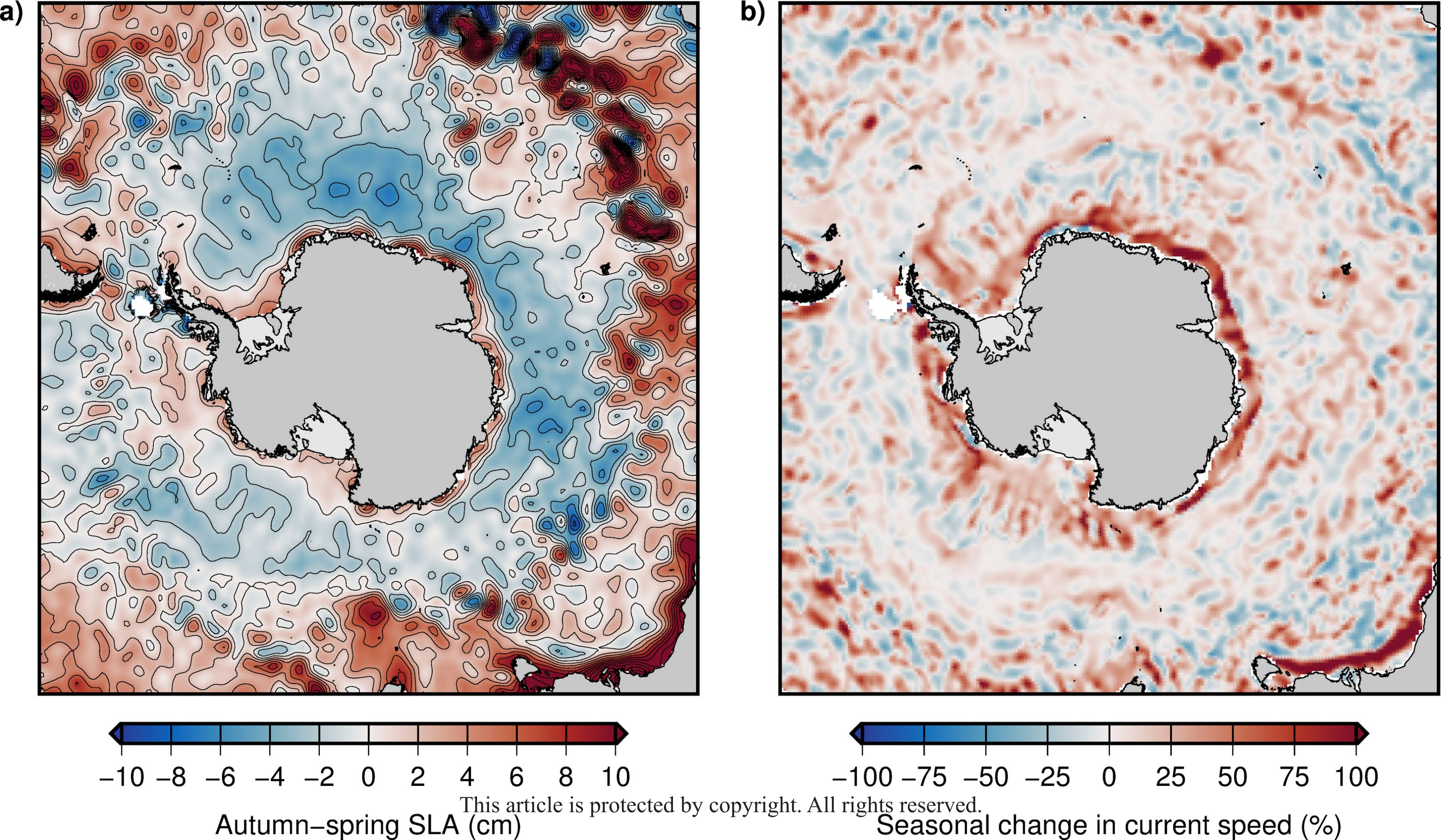
a)
b)
−10 −8 −6 −4 −2 0 2 4 6 8 10
Autumn−spring SLA (cm)
−100 −75 −50 −25 0 25 50 75 100
Seasonal change in current speed (%)

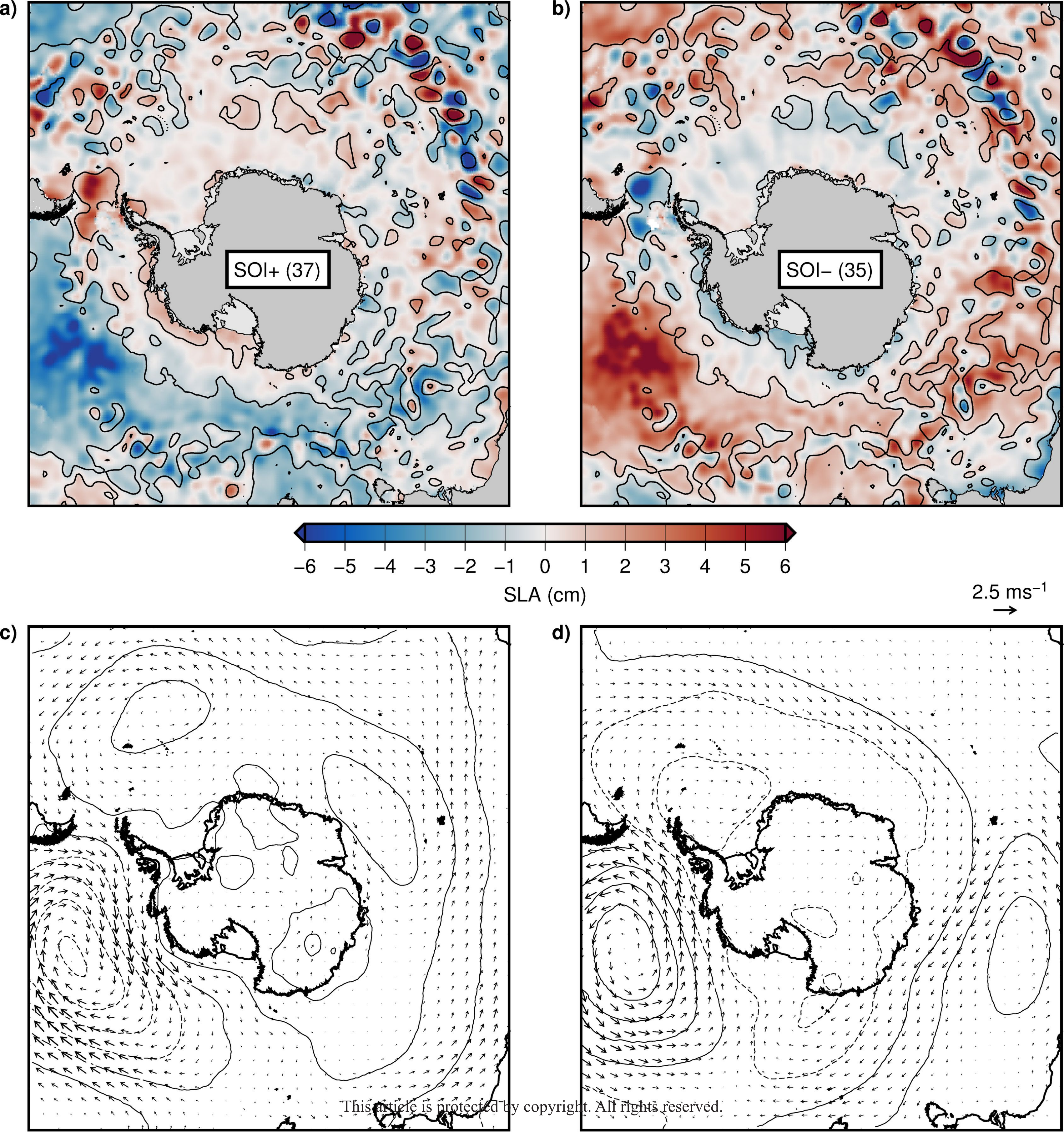
a)
SOI+ (37)
b)
SOI– (35)
−6 −5 −4 −3 −2 −1 0 1 2 3 4 5 6
SLA (cm)
2.5 ms^{-1}
c)
d)

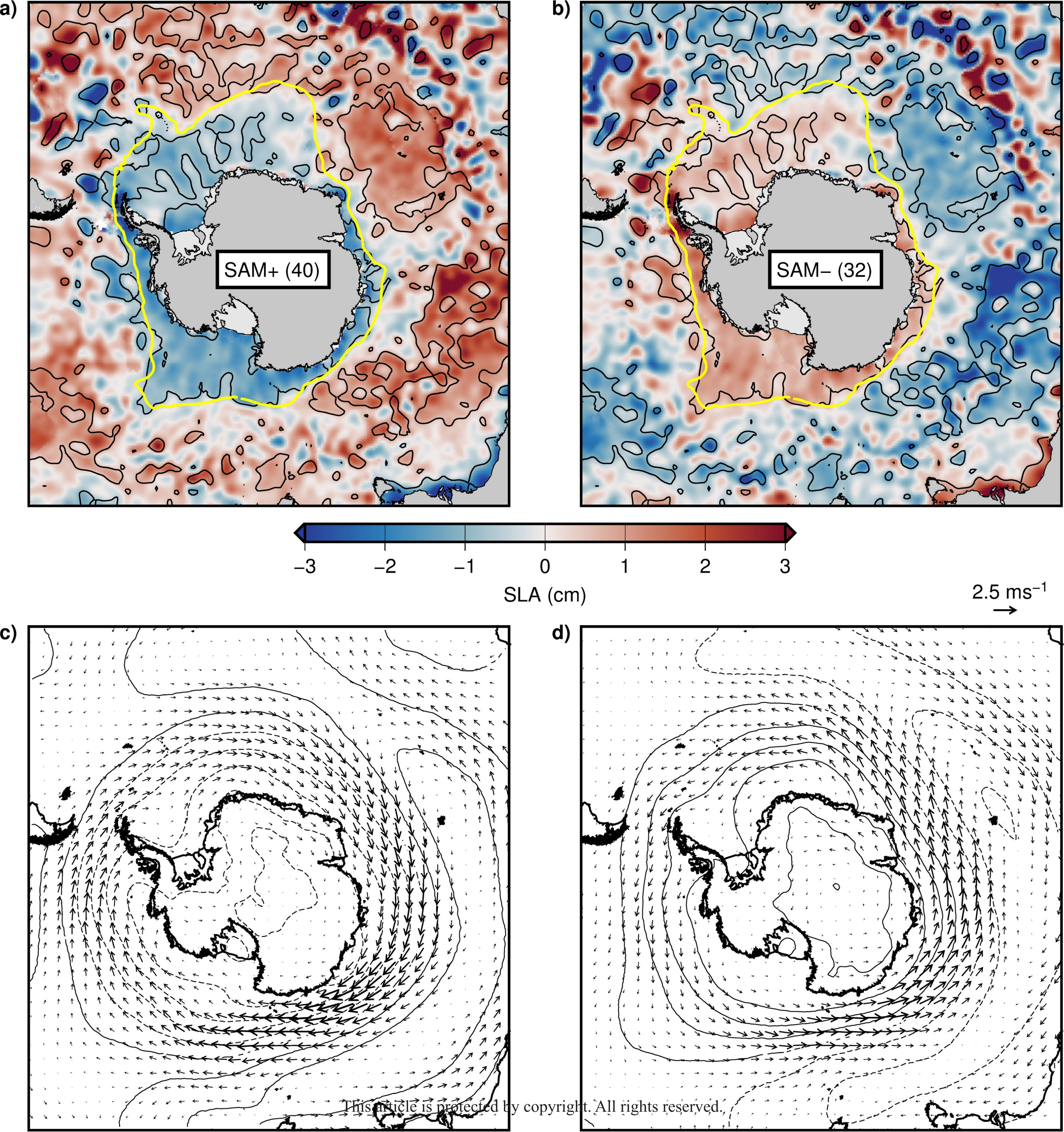
a)
b)
SAM+ (40)
SAM− (32)
−3
−2
−1
0
1
2
3
SLA (cm)
2.5 ms⁻¹
c)
d)

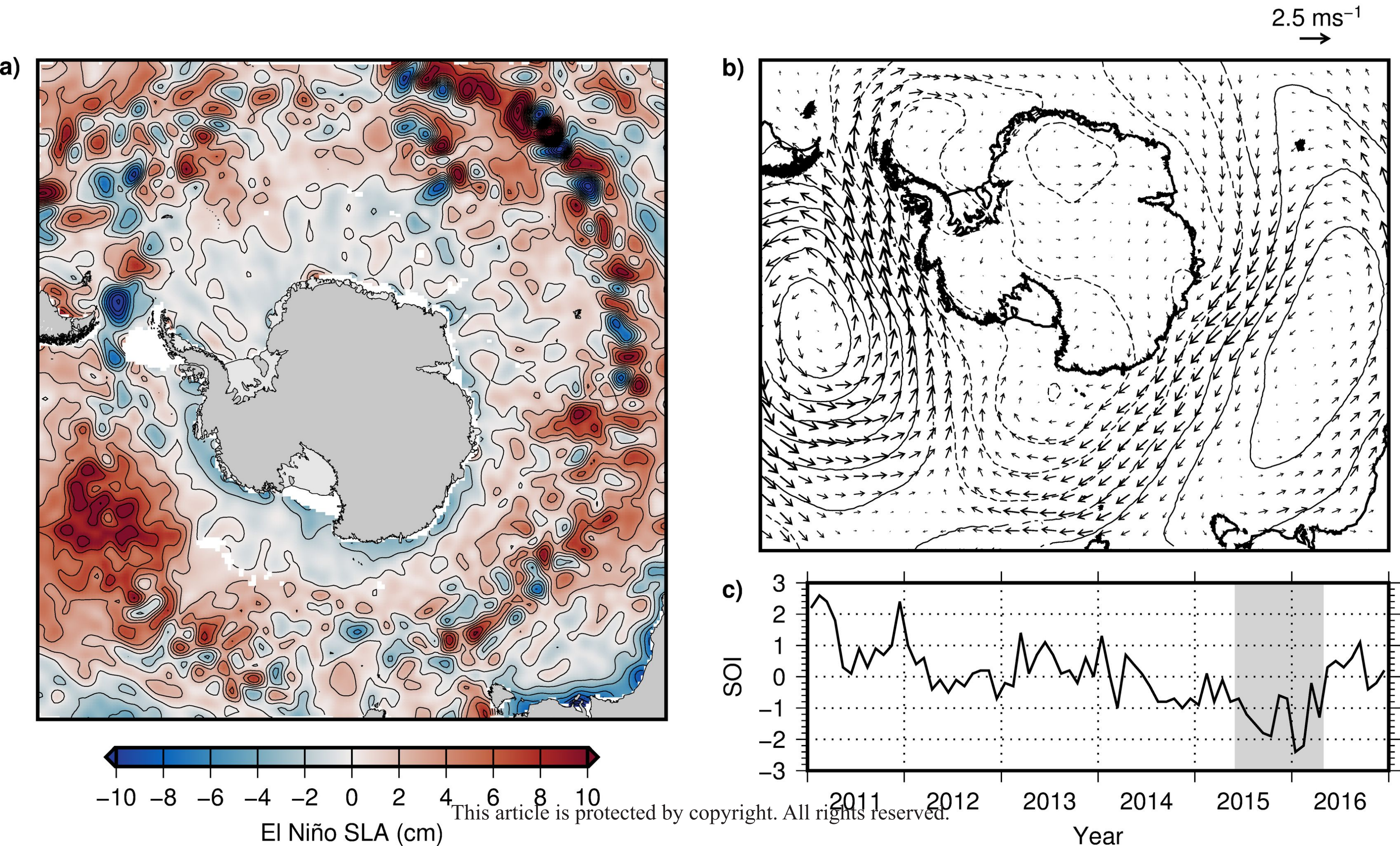
a)
b)
c)
2.5 ms−1
−10 −8 −6 −4 −2 0 2 4 6 8 10
El Niño SLA (cm)
SOI
3
2
1
0
−1
−2
−3
2011 2012 2013 2014 2015 2016
Year